BEAM-SQUINT AWARE CHANNEL ESTIMATION FOR DUAL-WIDEBAND
RIS-AIDED MASSIVE MIMO

A THESIS SUBMITTED TO
THE GRADUATE SCHOOL OF NATURAL AND APPLIED SCIENCES
OF
MIDDLE EAST TECHNICAL UNIVERSITY

BY

ONUR YILMAZ

IN PARTIAL FULFILLMENT OF THE REQUIREMENTS
FOR
THE DEGREE OF MASTER OF SCIENCE
IN
ELECTRICAL AND ELECTRONICS ENGINEERING

SEPTEMBER 2023

Approval of the thesis:

**BEAM-SQUINT AWARE CHANNEL ESTIMATION FOR
DUAL-WIDEBAND RIS-AIDED MASSIVE MIMO**

submitted by **ONUR YILMAZ** in partial fulfillment of the requirements for the degree of **Master of Science in Electrical and Electronics Engineering Department, Middle East Technical University** by,

Prof. Dr. Halil Kalıpçılar
Dean, Graduate School of **Natural and Applied Sciences** _____

Prof. Dr. İlkay Ulusoy
Head of Department, **Electrical and Electronics Engineering** _____

Assist. Prof. Dr. Gökhan Muzaffer Güvensen
Supervisor, **Electrical and Electronics Engineering** _____

Examining Committee Members:

Prof. Dr. Sinan Gezici
Electrical and Electronics Engineering, Bilkent University _____

Assist. Prof. Dr. Gökhan Muzaffer Güvensen
Electrical and Electronics Engineering, METU _____

Prof. Dr. Ali Özgür Yılmaz
Electrical and Electronics Engineering, METU _____

Prof. Dr. Cenk Toker
Electrical and Electronics Engineering, Hacettepe University _____

Assoc. Prof. Dr. Ayşe Melda Yüksel Turgut
Electrical and Electronics Engineering, METU _____

Date: 01.09.2023

I hereby declare that all information in this document has been obtained and presented in accordance with academic rules and ethical conduct. I also declare that, as required by these rules and conduct, I have fully cited and referenced all material and results that are not original to this work.

Name, Surname: Onur Yılmaz

Signature   :

ABSTRACT

BEAM-SQUINT AWARE CHANNEL ESTIMATION FOR DUAL-WIDEBAND RIS-AIDED MASSIVE MIMO

Yılmaz, Onur

M.S., Department of Electrical and Electronics Engineering

Supervisor: Assist. Prof. Dr. Gökhan Muzaffer Güvensen

September 2023, 73 pages

This study introduces a novel beam-squint aware (BSA) channel estimation method for reconfigurable intelligent surface (RIS)-aided frequency- and spatial-wideband (dual wideband) massive multiple-input multiple-output (MIMO) systems in millimeter wave (mmWave) frequency bands. The focus of our proposed method is on estimating slowly-varying angle and delay parameters, while effectively capturing fast-changing channel gains. For this purpose, we adopted both the slow-time parameter estimation (ST-PE) mode and the fast-time parameter estimation (FT-PE) mode within a coherence time. During the ST-PE mode, we propose novel BSA approach for estimating angle of arrivals (AoA) at the base station (BS). Subsequently, we employ a BSA and efficient joint orthogonal matching pursuit (OMP) algorithm to estimate the cascaded angle-delay pairs. On the other hand, the FT-PE mode involves a BSA subspace least square (LS) estimation method to estimate the channel gains. A notable feature of our proposed methods is their consideration of the amplitude-phase coupling constraint inherent in practical RIS structures, which enhances the realism of the channel estimation process. Through simulations, superior performance of our proposed estimation method is demonstrated in terms of normalized mean square er-

ror (NMSE) compared to existing approaches. Our findings highlight the potential of the BSA channel estimation method to optimize the performance of RIS-enabled massive MIMO systems.

ÖZ

ÇİFT GENİŞ BANTLI RIS DESTEKLİ BÜYÜK MIMO SİSTEMLERİNDE HÜZME ŞAŞMASINA DUYARLI KANAL KESTİRİMİ

Yılmaz, Onur

Yüksek Lisans, Elektrik ve Elektronik Mühendisliği Bölümü

Tez Yöneticisi: Dr. Öğr. Üyesi. Gökhan Muzaffer Güvensen

Eylül 2023 , 73 sayfa

Bu çalışma, milimetrik dalga (mmWave) frekans bandında yeniden yapılandırılabilir akıllı yüzey (RIS) destekli frekans ve uzamsal geniş bant büyük çoklu girdili ve çıktılı (MIMO) sistemler için hüzme şaşmasına duyarlı (BSA) yeni bir kanal kestirim yöntemini tanıtmaktadır. Önerdiğimiz yöntemin odak noktası, hızlı değişen kanal kazançlarını etkili bir şekilde yakalarken, yavaş değişen açı ve gecikme parametrelerini tahmin etmektir. Bu amaçla, tutarlılık süresi içinde hem yavaş zamanlı parametre tahmini (ST-PE) modunu hem de hızlı zamanlı parametre tahmini (FT-PE) modunu benimsedik. ST-PE modu sırasında, baz istasyonuna (BS) varış açısını (AoA) tahmin etmek için yeni bir BSA yaklaşımı öneriyoruz. Ardından, açı-gecikme çiftlerini tahmin etmek için BSA ve verimli ortak ortogonal eşleştirme takip (OMP) algoritması kullanıyoruz. Öte yandan, FT-PE modu, kanal kazançlarını tahmin etmek için bir BSA alt uzayı en küçük kareler (LS) tahmin yöntemini içerir. Önerdiğimiz yöntemlerin dikkate değer bir özelliği, pratik RIS yapılarında bulunan ve kanal tahmin sürecinin gerçekçiliğini artıran genlik ve fazı birbirini etkilemesini dikkate almalarıdır. Simülasyonlar aracılığıyla, önerilen tahmin yöntemimizin üstün performansı, mev-

cut yaklaşımlara kıyasla normalleştirilmiş ortalama karesel hata (NMSE) açısından gösterilmiştir. Bulgularımız, RIS özellikli büyük MIMO sistemlerinin performansını optimize etmek için BSA kanal kestirim yönteminin potansiyelini vurgulamaktadır.

Anahtar Kelimeler: kanal kestirimi, uygulanabilir RIS, uzaysal seçicilik etkisi

To my family and who believed in me...

ACKNOWLEDGMENTS

First and foremost, I would like to express my sincere gratitude to my supervisor, Dr. Gökhan Muzaffer Güvensen for his unwavering support since the very beginning. His invaluable time and genuine interest in my work have been instrumental in shaping this study. Without his continuous guidance and insightful advice, this research would not have been possible. I feel truly privileged to have been a graduate student under his mentorship.

I would like to extend my special thanks to Hakan Özen, who has been an exceptional collaborator and a tremendous help throughout my research. His support and willingness to share his vast knowledge and experience have been invaluable in advancing my studies. I am deeply grateful for his constant guidance and assistance in every aspect of my work.

Furthermore, words cannot adequately express my gratitude for the support of my family. My parents, Binnur Yılmaz, my sister, Özge Altuğ, and my brother, Mert Yılmaz, have been the pillars of my journey. Their dedication and unwavering belief in my academic pursuits have been the driving force behind my achievements from the first day.

I would like to express my gratitude to all my colleagues, whose contributions, too numerous to list here, have always been by my side throughout this work.

And lastly, I would like to reserve the most special thanks for my dear prospective wife, İrem Ertem (Yılmaz). Throughout this journey, you have shown incredible patience and resilience, standing by my side during the most challenging times, offering me the utmost support. You've never once wavered in your love, gifting me the most beautiful of emotions. No amount of gratitude can truly express how deserving that person is of the very best in everything.

TABLE OF CONTENTS

LIST OF TABLES

TABLES

LIST OF FIGURES

FIGURES

LIST OF ABBREVIATIONS

RIS   Reconfigurable Intelligent Surfaces

MIMO   Multiple-input multiple-output

mmWave   Millimeter wave

ST-PE   Slow-time parameter estimation

FT-PE   Fast-time parameter estimation

AoA   Angle of arrival

AoD   Angle of departure

BS   Base station

OMP   Orthogonal matching pursuit

MOMP   Modified orthogonal matching pursuit

LS   Least square

LMSSE   Linear minimum mean squared-error

CSI   Channel state information

BSE   Beam-squint effect

BSA   Beam-squint aware

CS   Compressed-sensing

OFDM   Orthogonal frequency-division multiplexing

LOS   Line-of-sight

ULA   Uniform linear array

UPA   Uniform planar array

UE   User equipment

MPC   Multipath cluster

VAD   Virtual angular domain

ADSP   Angle-delay scaling property

IPR	Iterative phase refinement
SNR	Signal-to-noise ratio
SINR	Signal-to-interference and noise ratio
NMSE	Normalized mean square error
CDF	Cumulative distribution function
RMSE	Root mean square error
WRMSE	Weighted root mean square error

CHAPTER 1

INTRODUCTION

1.1 Motivation

Conventional wireless communication takes place within an unpredictable and stochastic propagation environment. This environment can bring about difficulties such as signal weakening, strengthening, distortion, and even signal obstruction, which might lead to communication being infeasible under certain circumstances. Over the years, substantial efforts have been directed toward the advancement of sophisticated signal processing algorithms, such as adaptive modulation, coding, equalization, etc. These techniques are commonly implemented either at the transmitter or receiver end to enhance the signal quality. Nevertheless, they largely accept the wireless channel as it is and strive to alleviate its impacts. On the other hand, within today's technological landscape, the demand for wireless communication has escalated considerably. The number of mobile users is on the rise, and applications like virtual reality are rapidly gaining worldwide traction. As these trends lead to heightened demands on network traffic, achieving swifter and more efficient communication becomes an absolute necessity. All these have guided research efforts and have recently made it essential to incorporate effective channel optimization into communication scenarios. The goal is to transform the wireless channel from a passive conduit into a beneficial element in communication systems, capitalizing on the ability to manipulate its properties. It is within this context that the concept of RIS has emerged [2].

RIS, also known as Intelligent Reflecting Surfaces, is a technology composed of artificially engineered arrays of electromagnetic elements. Each of these reflecting elements is able to shift the phase of the impinging signal at low cost and complex-

ity [3]. RIS distinguishes itself by its distinctive feature that its reflective attributes can be dynamically configured in real-time through integrated electronic circuitry [4]. This dynamic adaptability of RIS enables it to actively manipulate signal propagation characteristics making the radio environment smart and controllable [5].

RIS technology, in terms of its working principle, shares similarities with traditional amplify and forward relays. Therefore, understanding how it differs from existing technology is crucial for gaining a better understanding of why RIS technology is promising. When looking at a communication system from the perspective of its two ends, the source and destination points, both have the functionality of relaying signals from the source to the destination. Additionally, one of their main objectives is to provide service to users who cannot see the source point. However, these two technologies differ in how they fulfill these functionalities. Relay systems, as is well known, receive signals like an ordinary receiver with their built-in RF components, then boost the signals using active elements and forward them towards the destination, acting like a regular transmitter. This approach involves RF components and active elements, resulting in higher power consumption. On the other hand, RIS technology is a surface that doesn't require any RF components. This surface reflects incoming signals according to the current phase shift design. In other words, RIS technology can achieve its goals without RF components and can operate in a more power-efficient manner compared to relays. Furthermore, while relay systems inevitably require full-duplex operation when simultaneously receiving and transmitting signals, which leads to self-interference issues, RIS only acts as a passive surface and can achieve full-duplex operation without encountering such problems. Finally, RIS technology's dynamic reconfigurability feature allows real-time updates of beamformer designs, further setting it apart from relay systems. While this study may not cover all aspects, existing literature has compared the two technologies in terms of performance and shown that RIS technology outperforms relay systems in various scenarios [6].

In its common usage scenario, RIS is employed within Multiple-Input Multiple-Output (MIMO) systems to establish alternative paths when the direct link between users is obstructed by the surrounding environment. An illustrative example of this is depicted in Figure 1. Additionally, properly configured RIS can enhance signal
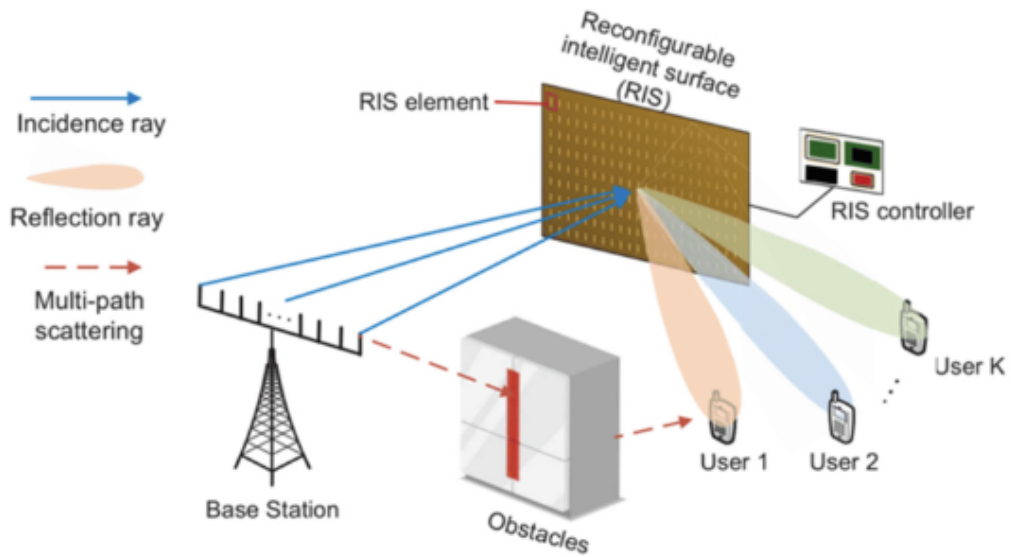
Figure 1.1: Illustration of typical RIS usage scenario [1].

strength at the receiving end. Studies show that, with N reflecting elements, RIS can achieve a power gain of $O(N^2)$ [7]. However, realizing the full potential of the RIS concept necessitates access to channel state information (CSI). RIS reflection settings need to be guided by this information to counterbalance unfavorable channel effects. However, in the context of RIS-assisted MIMO systems, channel estimation presents certain challenges [8]. Firstly, RIS is intended to be mainly passive to ensure cost-effective operation. Consequently, this task involves estimating cascaded channels between Base Stations (BS)-RIS and RIS-users, rather than the channels individually. Secondly, the typically large dimensions of the system further increase the complexity of estimating cascaded channels.

In addition to them, another challenge within the context of channel estimation of the RIS-assisted MIMO system pertains to the phenomenon commonly referred to as the Beam-Squint Effect (BSE). With the increase of array dimensions, the difference in the sampling time among antennas becomes comparable with the symbol duration. This scenario inherently results in dissimilar symbols being received by different antennas across varying time instances. Accordingly, in the frequency domain, it causes frequency-dependent channel angle of arrival (AoA), and angle of departure (AoD). In this case, if the angular differences are not taken into account and beamforming

is performed without considering them, the beams observed by the receiver will be perceived as having changed angles depending on the frequency. In other words, the beams intended by the transmitter will deviate from their original directions. This deviation and shifting in the beams is named as beam-squint. It is crucial to correctly address and mitigate this effect, otherwise, the channel estimation will suffer severe performance losses [9], [10].

1.2 Related Literature

In the literature, with the emergence of RIS, there has been a tendency to consider the channel as perfect in RIS-based system designs [11]. However, the importance of channel estimation and its challenging nature has been emphasized at the same time, leading to considerable research efforts in this area until today. These efforts can be categorized into two groups based on how RIS is architectured: semi-passive and fully-passive approaches [12]. In the first group, RIS incorporates limited active sensing elements placed on intelligent surfaces. These sensing elements allow signal processing capabilities on the RIS, enabling separate channel estimations for the BS-RIS and RIS-user channels. The second group, on the other hand, considers a fully passive RIS, constructed solely with passive elements, leading to investigations of different scenarios. In this group, since no signal processing can be performed on the RIS, a cascaded approach is adopted for channel estimation, sequentially estimating the BS-RIS and RIS-user channels. While, [13] and [14] studies focused on separate channel estimations for RIS-aided systems within the first group, it is observed that employing a fully-passive RIS structure could achieve higher channel estimation performance at a lower cost by [15], leading to a considerable shift in the literature towards this approach. Studies adopting fully-passive RIS structures and performing cascaded channel estimation started with simple channel models, applying commonly used Least-Square (LS) and Linear Minimum Mean Squared-Error (LMMSE) methods [16], [17]. They suggested the estimation of the instantaneous channel in time sequentially together with the on-off strategy, while the joint optimization of the pilot sequences and the RIS reflection coefficients was suggested by [18]. Subsequently, studies [19], [20] introduced element-grouping to reduce the

4

number of pilot sequences required. Nevertheless, all these pioneering studies still require a significant number of pilot sequences. This is because these methods need rank-efficient channel matrices to avoid ambiguities, and to ensure this, at least as many observations as unknown channel parameters are needed which is hard to sustain due to huge dimensions. Especially in high-frequency bands such as mmWave, where severe path losses and occasional blockages create a limited scattering environment [21], the channel becomes rank deficient, causing these methods to lose their validity. To address the challenge of accurate channel estimation and high pilot overhead, studies [22], [23], [24] transformed RIS-aided system channel estimation into a sparse signal recovery problem, applying widespread Compressed-Sensing (CS) methods. In studies [22] and [23], the OMP algorithm was employed in the angular domain to solve the BS-RIS-user cascaded channel estimation problem, providing relatively low-complexity solutions. In study [24], a novel channel estimation protocol within the framework of compressed sensing was proposed. It utilized OMP to sparsely estimate slowly changing angle parameters and employed the LS method for rapidly changing gain parameters, achieving significant complexity reductions. However, it is worth noting that the methods adopting compressed sensing generally treat the channel as narrowband, neglecting the wideband effects of frequency and spatial variations. Additionally, these methods often idealize RIS elements, neglecting practical concerns in their implementation.

In modern communication systems, the need for high-speed data transmission makes the use of broadband inevitable. Therefore, channel estimation in frequency-selective channels has become a significant step in the RIS literature. Initially, studies [19], [20] addressed frequency selectivity in RIS-aided systems and meets Orthogonal Frequency-Division Multiplexing (OFDM) with channel estimation problem. However, as mentioned before, these studies used LS-based methods, requiring impractical pilot durations. In study [25], an important advancement in the RIS literature was made by considering CS-based channel estimation with OFDM. It exploited the common channel sparsity across all subcarriers, utilizing OMP in the angular domain while jointly exploiting signals received from all subcarriers. To address OMP's power leakage problem caused by off-grid angles known as the grid-mismatch problem, the dictionary matrix was redundantly designed with fine resolution, increasing

5

the complexity of solving the problem. [26] proposed a different solution to the grid problem of OMP. It suggested reducing user channel angles into groups by performing downlink transmission before finding fine angles at the BS and transmitting this information back to the BS. Although this reduced complexity in combat for OMP grid-mismatch, it introduced a relatively complex protocol and time loss. The last two studies focused on the assumption of line-of-sight (LOS) dominance for RIS and BS, restricting mobility in the environment. In contrast, study [13] introduced a different RIS approach by designing a twin-structured RIS and using OFDM, thereby promoting diverse RIS designs in the literature. Moreover, unlike other OFDM-based works, it considered practical concerns in the RIS elements. Although these studies worked on OFDM-based frequency-wideband channel estimation, they did not consider spatial wideband effects, leaving the dual-wideband channel estimation problem unexplored. In RIS-assisted systems using wideband and operated by high-dimensional arrays, the beam-squint effect is inevitable, and studies that do not consider this effect may suffer significant performance losses [9]. The literature offers only a limited number of studies that address this topic and perform channel estimation considering the dual-wideband effect. Studies [27] and [28] emerged independently around the same time, both adopting CS-based techniques to handle the dual-wideband effect and performing cascaded channel estimation. Study [27] considered BS with a single antenna, neglecting BS-side AoA estimation. Similarly, study [28] treated the BS-RIS link as LOS dominant, restricting mobility and focusing only on the RIS-user channel. These two studies left a gap in the literature by not considering practical concerns related to RIS elements. Study [29] attempted to fill this gap by proposing a deep learning-based technique for dual-wideband channel estimation. However, it only incorporated practical approximations in the phases of RIS elements, assuming their amplitudes to be constant. Another common aspect of these wideband studies is assuming constant channel gains for each OFDM symbol, whereas, channel gains on OFDM symbols can decorrelate over time due to their long duration. The summary of the existing work in the literature is presented in table 1.1.

Table 1.1: Existing works on channel estimation in the RIS-aided systems

Papers	[19, 20]	[22–24]	[25, 26]	[27, 28]	[29]	This Work
Sparse Signal Recovery	✗	✓	✓	✓	✓	✓
Frequency Wideband	✓	✗	✓	✓	✓	✓
Spatial Wideband	✗	✗	✗	✓	✓	✓
Practical RIS Design	✗	✗	✗	✗	✓	✓
MPC Gain Decorrelation	✗	✗	✗	✗	✗	✓

1.3 Contributions and Novelties

It can be summarized that in the literature CS-based methods for estimating cascaded BS-RIS-user channels are popular in general. However, there seems to be relatively little emphasis on considering the practical effects of RIS elements in channel estimation methodologies. While frequency-selective channel estimation under wideband effects has been widely studied, the investigation of wideband spatial effects has been limited. Additionally, in wideband channel estimation studies using OFDM, it is observed that the channel gains on OFDM symbols are assumed to be fully correlated, which may be insufficient in practice considering the long duration of OFDM symbols. To fill these research gaps, we propose a novel channel estimation method for dual wideband RIS-aided MIMO systems that explicitly considers the BSE, accounts for the amplitude-phase coupling constraint, and acknowledges the rapidly changing nature of channel gains. The key contributions of this work are summarized as follows:

- Proposed channel estimation addresses both the wideband frequency effect and spatial effect. These effects were incorporated into the system model, and the algorithms were designed to be aware of these.

- The proposed algorithm incorporates both sparse signal recovery and the basic LS method. We introduce a training scheme that considers the slow- and fast-time temporal characteristics of channel parameters. For the slowly changing channel parameters, we propose the BSA method for the BS-side AoA estimation first, followed by the CS-based method, specifically the efficient OMP

algorithm for cascaded angle-delay pairs. These algorithms are infrequently operated to ensure computational efficiency. On the other hand, for rapidly changing channel gains, we apply the widely used LS method.

- In the proposed OMP algorithm, to address the grid-mismatch problem without increasing computational complexity, we adopt a novel approach. First, we create a coarse dictionary to identify the coarse angles and delay pairs. Then, we iteratively refine the previously generated dictionary around the coarsely estimated cascaded angle-delay pairs. This refinement process allows us to search for cascaded angle and delay parameters more precisely. By running OMP with a reduced-size dictionary, we can effectively reduce complexity while accurately estimating the cascaded parameters.

- The correlation between channel gains over OFDM symbols is considered, and the proposed algorithms are designed to combat this effect. We modeled fully correlated and decorrelated channels and tested the algorithms under these conditions.

- All these studies are conducted using passive RIS elements, thereby avoiding extra hardware and operational costs. Additionally, in the RIS design, practical RIS concerns are taken into account, where the phase and amplitude coupling of the reflecting elements is added in the reflection pattern design. The developed algorithms are also demonstrated to work effectively with this practical RIS configuration.

1.4 Notation and Outline

Within this section, we introduce the notations essential for the mathematical operations employed consistently throughout this thesis. To differentiate quantities, lowercase letters (e.g., x), and lowercase boldface letters (e.g., $\mathbf{x}$) are reserved for scalars and vectors, while uppercase boldface letters (e.g., $\mathbf{X}$) signify matrices. The complex conjugate of scalar x is designated as x^*, and its magnitude is represented as $|x|$. Furthermore, the determinant, inverse, transpose, and Hermitian of matrix $\mathbf{X}$ are shortly denoted by $|\mathbf{X}|$, $\mathbf{X}^{-1}$, $\mathbf{X}^T$ and $\mathbf{X}^H$, respectively. To specify a specific element

in matrix $\mathbf{X}$, $[\mathbf{X}]_{(i,j)}$ refers to the entry in the ith row and j^{th} column. Additionally, $[\mathbf{X}]_{(i,:)}$ and $[\mathbf{X}]_{(:,j)}$ indicate the ith row and j^{th} column of matrix $\mathbf{X}$, respectively. In a similar way, $[\mathbf{x}]_{(i)}$ refers to the ith element of vector $\mathbf{x}$. For vectors, $\|\mathbf{x}\|$ signifies the Euclidean norm, while $\|\mathbf{X}\|_F$ represents the Frobenius norm of matrix $\mathbf{X}$. Complex Gaussian random variables possessing a mean of μ and variance of σ^2 are properly denoted by $\mathcal{CN}(\mu, \sigma^2)$, while $\mathcal{CN}(\mathbf{x}, \mathbf{R})$ symbolizes complex Gaussian random vectors characterized by a mean of μ and covariance matrix $\mathbf{R}$. Employing the symbol $\odot$ denotes the element-wise Hadamard product between matrices, and $\otimes$ signifies the Kronecker product of two matrices. The Kronecker delta function is represented as δ_{ij}. Expectation is denoted by $\mathbb{E}\{\cdot\}$, the trace operator is represented by $\mathrm{Tr}\{\cdot\}$, and $\mathrm{Toeplitz}\{\mathbf{u}^H\} = \mathbf{U}$ is an operator that maps the column vector $\mathbf{u} \in \mathbb{C}^{M \times 1}$ to a matrix $\mathbf{U} \in \mathbb{C}^{M \times M}$, with $\mathbf{U}$ exhibiting the characteristic $[\mathbf{U}]_{(1,:)} = \mathbf{u}^H$.

In the upcoming sections, we will briefly look at the overall system first. A detailed understanding of the system will be discussed in chapter 2, where we will introduce the system model and the fundamental protocol underlying the channel estimation methods. Chapter 3 and 4 will then delve into explaining how channel estimation works. Chapter 3 will primarily focus on methodologies developed towards estimating the slowly varying parameters of the channel, while chapter 4 will delve into channel estimation techniques tailored for rapidly changing parameters, completing the entire channel estimation process. Chapter 5 is dedicated to the presentation of performance results, encompassing measurement metrics, numerical values of the system, and simulation outputs. Ultimately, chapter 6 will draw the study to a close by providing conclusive insights.

CHAPTER 2

SYSTEM MODEL

We focus on the uplink transmission scenario in mmWave MIMO systems. To enhance communication performance, we deploy a single RIS structure with purely passive reflecting elements within the channel. Both the BS and the RIS employ a uniform linear array (ULA) configuration for their antenna arrays. Multi-antenna is used at the BS and RIS and the number of antennas can be denoted by M and N respectively. The User Equipment (UE) operates with a single antenna in the far-field region on the other hand. We assume that there is no direct link between the BS and the UE. However, the proposed estimation method can easily be adapted to estimate the direct link if it is available. In such a scenario, we can divide the estimation process into two stages. In the first stage, RIS can be turned off to estimate the direct link. In the second stage, we apply the proposed method to estimate the composite channel, thereby capturing the entire channel behavior [30]. Furthermore, the angles and delays are considered as slowly-varying parameters, while the channel gains are considered as fast-varying parameters in our model. Finally, it is important to address one last point regarding the antenna array type. In the literature, the use of ULA-type antennas is quite common in RIS-aided communication systems. Therefore, in the scope of this study, the antenna array type has been considered as ULA. However, when we think about scenarios where RIS is deployed as a 2-D surface, working with uniform planar array (UPA) type antenna arrays becomes inevitable. At this point, we can easily conclude that this study can be readily extended to systems using UPA-type antenna arrays. In such a scenario, while the delay and gains from the channel components remain the same, the angle components need to be defined in two different axes, both azimuth and elevation. Subsequently, by defining the array manifold response along both azimuth and elevation, we obtain the array response for UPA-

11

type arrays. With this array response, along with updated signal models and channel estimation methods, we can expect to perform channel estimation within the context of UPA-type arrays.

2.1 Channel Estimation Protocol

Considering the mobility of the environment and the locations of communication endpoints, it can be anticipated that channel angles change relatively slowly, while change in the channel gains is much faster. This disparity in the rate of change requires considering separate coherence block timings for angles and gains. To address this distinction, the coherence block definition can be remarked as the intervals where the angles remain relatively stable while gains undergo rapid changes [31], [32]. This concept can also be referred to as *angular coherence* blocks. The communication protocol we propose is based on dividing time into these coherence blocks. As shown in figure 2.1, these coherence blocks consist of a time slot T_c which encompasses T_c OFDM symbol blocks. The beginning of each coherence block is reserved for training, and this phase can be interchangeably referred to as the *training mode* or the *ST-PE mode*. During this training time, the user sends consecutively pilot sequences for a duration $T \ll T_c$ to launch the ST-PE mode channel estimation. This way, the slowly changing angle and delay parameters of the channel are estimated, and there is no need for repeating this estimation assuming stability during these blocks. This strategy significantly reduces the need for frequent angle and delay estimation compared to gain-based estimation, resulting in time and computational efficiency. After completing the angle and delay estimation task, the coherence blocks are allocated for data transmission. This section on the other hand can be called the *data mode* or the *FT-PE mode* where users engage in communication while simultaneously estimating the channel gains. For this estimation, the user selects only a small subset of subcarriers relative to the data transmission and employs the FT-PE mode channel estimation mechanism. Due to the rapid changes in channel gains, the user employs the FT-PE mode at each time instance. As will be explained in subsequent sections, adopting a relatively simpler method for gain estimation proves advantageous for this mode, enhancing efficiency.

12
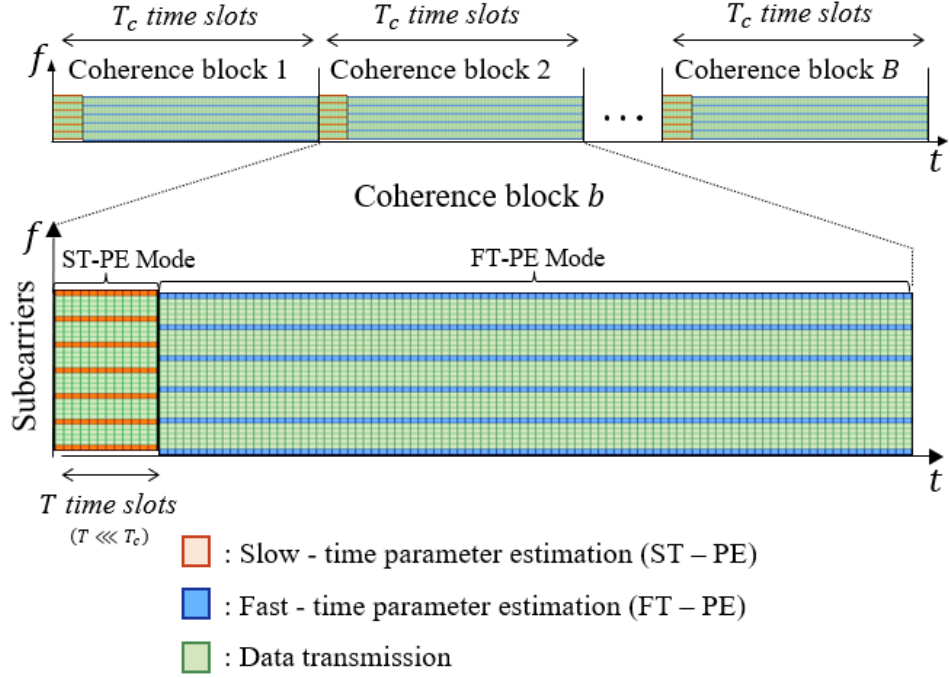
Figure 2.1: Proposed channel estimation frame structure

In both the FT-PE and ST-PE estimation, the RIS is dynamically configured to facilitate ongoing communication in line with its adaptable nature. As depicted in Figure 2.2, within the ST-PE mode, the RIS is tailored to scan the intended sector across T consecutive time instances. This scanning mechanism ensures the aggregation of information from various angles within the intended sector. This enables the estimation of angles and delays at the BS. Conversely, in the FT-PE mode, where angles were already estimated and remain fixed, the RIS is reconfigured to align with the estimated angles. This alignment guarantees that the signals transmitted by the user reach the BS through the predetermined angles, thereby enhancing the efficacy of the estimation process.

2.2 RIS-Aided Uplink Transmission Under Beam-Squint

In the mmWave communication scenario, the received signal $\mathbf{y}_{k,n} \in \mathbb{C}^{M \times 1}$ at the BS in the frequency domain for the kth subcarrier at the nth time instance within a

Figure 2.2: RIS configuration in proposed modes

coherence block can be expressed as [24]

$$\mathbf{y}_{k,n} = \mathbf{H}_{k,n} \operatorname{diag}(\boldsymbol{\phi}_n)\mathbf{h}_{k,n}x_{k,n} + \mathbf{n}_{k,n}, \tag{2.1}$$

for $k = 1, 2, \ldots, N_c$, $n = 1, 2, \ldots, T_c$, where N_c denotes the number of subcarriers and $x_{k,n}$ represe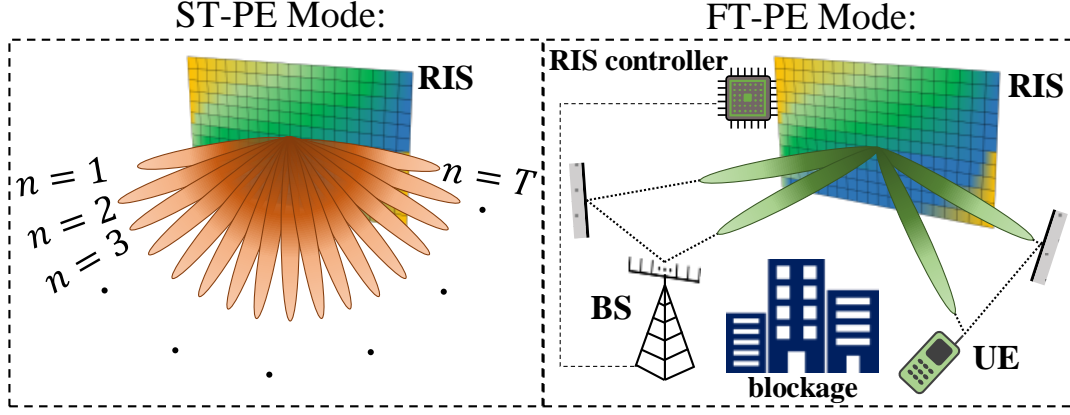nts the transmitted OFDM symbol of the user that satisfies $\mathbb{E}\{x_{k,n}x_{k',n'}^H\} = \delta_{kk'}\delta_{nn'}$. The matrix $\mathbf{H}_{k,n} \in \mathbb{C}^{M \times N}$ represents the frequency domain channel matrix between the BS and RIS, whereas $\mathbf{h}_{k,n} \in \mathbb{C}^{N \times 1}$ stands for the frequency domain channel vector between the RIS and user. $\boldsymbol{\phi}_n$ is the frequency-independent reflection coefficient matrix of the RIS which operates between BS and the user. $\mathbf{n}_{k,n} \in \mathbb{C}^{M \times 1}$ is a zero-mean complex random Gaussian noise vector that satisfies $\mathbb{E}\{\mathbf{n}_{k,n}\mathbf{n}_{k',n'}^H\} = N_0\mathbf{I}_M\delta_{kk'}\delta_{nn'}$.

The spatially sparse and dual-wideband BS-RIS and RIS-UE channels in the frequency domain for the kth subcarrier at the nth time instance can be represented by using the geometric channel model as [33], [34]

$$\mathbf{H}_{k,n} = \sum_{\ell=1}^{L} \overline{\gamma}_{\ell,n} \, \overline{\mathbf{u}}_k(\theta_\ell) \, \mathbf{u}_k^H(\varphi_\ell) e^{-i2\pi(f_k+f_c)\overline{\tau}_\ell}, \tag{2.2}$$

$$\mathbf{h}_{k,n} = \sum_{j=1}^{J} \gamma_{j,n} \, \mathbf{u}_k(\vartheta_j) e^{-i2\pi(f_k+f_c)\tau_j}, \tag{2.3}$$

14

In these channel expressions, L represents the number of multipath clusters (MPCs) between the BS and RIS, while J is the number of MPCs between the RIS and UE. $\overline{\gamma}_{\ell,n}$ and $\gamma_{j,n}$ are the complex channel gain for the ℓth and j^{th} MPC respectively. The channel angle components within these expressions are delineated as follows: $\theta_\ell = \sin\widetilde{\theta}_\ell$ is the directional sine of the AoA $\widetilde{\theta}_\ell$ at the BS, $\varphi_\ell = \sin\widetilde{\varphi}_\ell$ is the directional sine of the AoD $\widetilde{\varphi}_\ell$ at the RIS, and $\vartheta_j = \sin\widetilde{\vartheta}_j$ is the directional sine of the AoA $\widetilde{\vartheta}_j$ at the RIS. In a similar fashion, channel delay components are represented by $\tau_\ell \sim$ $Unif[0, \overline{\tau}_{\max})$ and $\tau_j \sim Unif[0, \tau_{\max})$ which are the propagation delay components from the RIS to the BS and from the UE to the RIS with the maximum propagation delays of $\overline{\tau}_{\max}$ and $\tau_{\max}$ respectively. W is the signal bandwidth and f_c is the center frequency. For a clearer understanding and visualization, the described system model and the explicitly shown channel components in the uplink communication scenario are presented in figure 2.3.
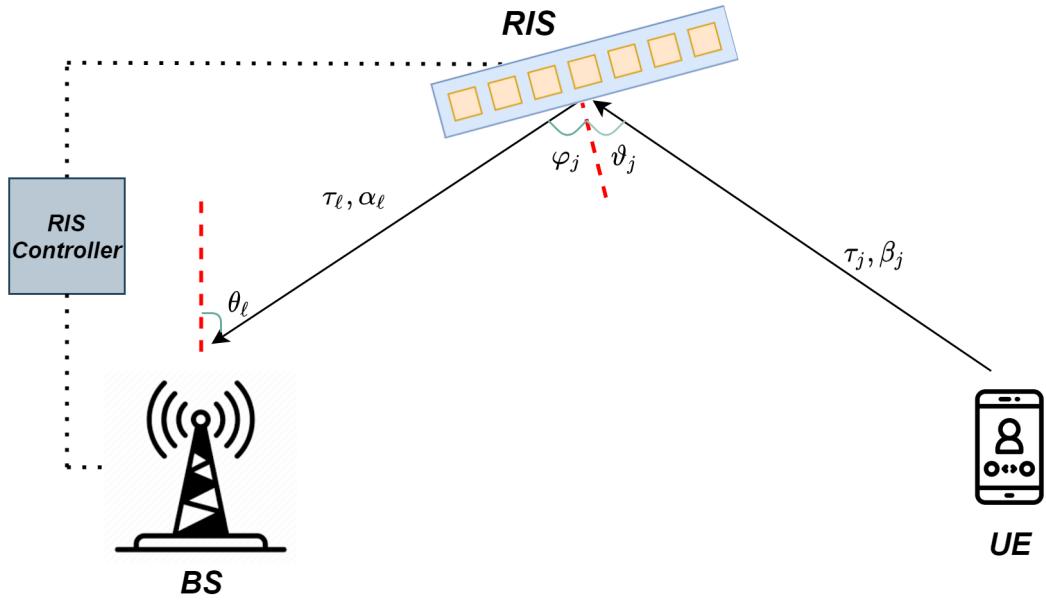

Figure 2.3: Described RIS-assisted mmWave communication system

Furthermore, the discrete frequency value of the kth subcarrier in baseband can be calculated based on the following

$$f_k = -\frac{W}{2} + (k-1)\frac{W}{N_c - 1},\qquad(2.4)$$

The spatial wideband array responses of the BS and RIS denoted by $\overline{\mathbf{u}}_k(\cdot) \in \mathbb{C}^{M\times 1}$

and $\overline{\mathbf{u}}_k(\cdot) \in \mathbb{C}^{M \times 1}$ can be expressed as [10]

$$\overline{\mathbf{u}}_k(\theta) = \left[1, e^{-i2\pi \frac{d_{\mathrm{BS}}}{\lambda_c} \theta \left(1+\frac{f_k}{f_c}\right)}, \ldots, e^{-i2\pi(M-1)\frac{d_{\mathrm{BS}}}{\lambda_c} \theta \left(1+\frac{f_k}{f_c}\right)}\right]^T, \qquad (2.5)$$

$$\mathbf{u}_k(\theta) = \left[1, e^{-i2\pi \frac{d_{\mathrm{RIS}}}{\lambda_c} \theta \left(1+\frac{f_k}{f_c}\right)}, \ldots, e^{-i2\pi(N-1)\frac{d_{\mathrm{RIS}}}{\lambda_c} \theta \left(1+\frac{f_k}{f_c}\right)}\right]^T, \qquad (2.6)$$

where d_{BS} and d_{RIS} is the antenna spacing at the BS and the element spacing at the RIS respectively, and λ_c is the corresponding wavelength for the operating center frequency.

The complex MPC gains between BS and RIS $\overline{\gamma}_{\ell,n}$, and RIS and UE $\gamma_{j,n}$ can be further expanded as [35]

$$\overline{\gamma}_{\ell,n} = \overline{\mu}_\ell e^{i\overline{\beta}_{\ell,n}} + \overline{\alpha}_{\ell,n}, \qquad (2.7)$$

$$\gamma_{j,n} = \mu_j e^{i\beta_{j,n}} + \alpha_{j,n}, \qquad (2.8)$$

where $\overline{\mu}_\ell$ and μ_j stand for the rician mean components, $\overline{\beta}_{\ell,n}$ and $\beta_{j,n}$ represent a random phase of the rician component which is uniformly distributed over 0 and 2π, $\overline{\alpha}_{\ell,n}$ and $\alpha_{j,n}$ are the random complex coefficient for the rayleigh component following the distribution of $\sim \mathcal{CN}(0, \overline{\sigma}_\ell^2)$ and $\sim \mathcal{CN}(0, \sigma_j^2)$ respectively. Therefore, the Rician factor for the ℓth MPC of $\mathbf{H}_k$ in (2.2) can be defined as $\overline{\kappa}_\ell \triangleq \overline{\mu}_\ell^2 / \overline{\sigma}_\ell^2$, and also the same definition can also be made for the jth MPC of $\mathbf{h}_{k,n}$ in (2.3) as $\kappa_j \triangleq \mu_j^2 / \sigma_j^2$.

2.3 Practical RIS with Amplitude-Phase Coupling

Contrary to the widespread assumption that default reflecting elements possess a fixed amplitude envelope, the amplitudes of RIS elements are influenced by their phases. This phenomenon is captured in the RIS literature as the *amplitude-phase coupling* of RIS elements. As demonstrated in [36], the amplitude tends to approach unity as the phase increases, however, energy loss on the RIS elements increases when

16

the phase approaches zero due to electromagnetic effects. This energy loss which can be in the form of as dielectric loss, metallic loss, and ohmic loss, leads to a reduction in the reflection amplitudes of RIS elements. Since this loss originates from the semiconductor device upon which the RIS is constructed, practical prevention is unfeasible Although the consideration of introducing amplifiers to counteract this loss arises, it contradicts the cost-efficiency principle of passive RIS, particularly within its fundamental scope. In the same study, the amplitude and phase coupling of the RIS, encompassing a variety of semiconductor devices, is modeled as follows [36]

$$\beta\left(\theta_m\right) = \left(1 - \beta_{\min}\right)\left(\frac{\sin\left(\theta_m - \phi_0\right) + 1}{2}\right)^{a_0} + \beta_{\min}, \qquad (2.9)$$

for $m = 1, 2, \ldots, N$ where $\beta_{\min} \geq 0, \phi_0 \geq 0$ and $a_0 \geq 0$ are the specific circuit-related constants and assumed to be same for all RIS elements. Moreover, β and θ_m represent the amplitude and phase of each RIS element such that

$$[\phi]_{(m)} = \beta\left(\theta_m\right) e^{j\theta_m}, \qquad (2.10)$$

When the amplitude is ideally taken as unity, this practical effect stemming from the nature of the RIS can lead to severe performance losses. Indeed [37] and [38] studies have highlighted these performance losses in RIS-aided localization applications when this effect is not considered. Therefore, it is essential to account for this effect when designing RIS phase shift configurations.

CHAPTER 3

SLOW-TIME PARAMETER ESTIMATION

At the beginning of each coherence block, the user's primary objective is to gather information about the channel. Therefore, the user performs ST-PE and estimates the slowly changing components of the channel, namely angles and delays. In the fully passive setup of the RIS, no signal processing takes place on the RIS itself, and the estimation is performed on the BS side. Hence, the user initially estimates the AoA at the BS, and then attempts to estimate the cascaded angles and delays formed between the UE to RIS, and RIS to BS. For this cascaded estimation, a CS-based technique is employed, leveraging the sparsity inherent to the mmWave frequency band. Additionally, the RIS beamforming is designed to dynamically adjust its beamforming to focus on a specific direction during each of the T consecutive time instances. The user transmits pilot symbol sequences over a fraction of subcarriers, particularly using $N_c^{(\text{s})}$ subcarriers out of the total N_c. Throughout T consecutive time instances, these pilot symbols are continuously transmitted.

Let $\mathcal{N}_c^{(\text{s})} \triangleq \left\{ 1, \frac{N_c}{N_c^{(\text{s})}-1}, \frac{2N_c}{N_c^{(\text{s})}-1}, \frac{3N_c}{N_c^{(\text{s})}-1}, \ldots, N_c \right\}$ denote the indexes of the subcarriers allocated for the ST-PE such that $|\mathcal{N}_c^{(\text{s})}| = N_c^{(\text{s})}$. The pilot sequences are known to the BS, therefore this allows us to assume that $x_{k,n} = 1 \ \forall k \in \mathcal{N}_c^{(\text{s})}, n \in \{1, 2, \ldots, T\}$ during the ST-PE mode without loss of generality. As a result, we can eliminate the information symbol $x_{k,n}$ in (2.1). Furthermore, by substituting (2.2) and (2.3) into (2.1), the received signal $\mathbf{y}_{k,n}$ in (2.1) can be expressed $\forall k \in \mathcal{N}_c^{(\text{s})}, n \in \{1, 2, \ldots, T\}$ as

$$\mathbf{y}_{k,n} \triangleq \sum_{\ell=1}^{L}\sum_{j=1}^{J}\gamma_{\ell,j,n} e^{-i2\pi(f_k+f_c)\tau_{\ell,j}}\big[(\boldsymbol{\phi}_n^{(\mathrm{s})})^T \mathbf{u}_k(\varrho_{\ell,j})\big]\overline{\mathbf{u}}_k(\theta_\ell) + \mathbf{n}_{k,n},$$

(3.1)

where $\gamma_{\ell,j,n} \triangleq \overline{\gamma}_{\ell,n}\gamma_{j,n}$ is the cascaded gain, $\tau_{\ell,j} \triangleq \overline{\tau}_\ell + \tau_j$ is the cascaded delay, and $\varrho_{\ell,j} \triangleq \vartheta_j - \varphi_\ell$ is the cascaded angle induced from UE to RIS and RIS to BS.

3.1 BS-Side AoA Estimation

ST-PE mode initially aims to estimate the BS side AoA, and in order to achieve this estimation at the BS, we extend the estimation methodology proposed in [24] and apply discrete Fourier transform (DFT) based technique with the beam-squint effect incorporated. Let $\mathbf{S}_k$ denote the wideband DFT matrix for the kth subcarrier

$$[\mathbf{S}_k]_{(m,n)} = e^{1i\frac{2\pi}{M}(m-1)(n-1)\left(1+\frac{f_k}{f_c}\right)}$$

(3.2)

$\forall m, n \in \{1, 2, \ldots, M\}$. Notice that $\mathbf{S}_k$ transforms into the conventional DFT matrix for the center subcarrier i.e. when f_k is equal to 0. Let us construct the matrix $\mathbf{Y}_k$ concatenating the observations in (2.1) over time slots for the kth subcarrier as

$$\mathbf{Y}_k \triangleq [\mathbf{y}_{k,1}, \mathbf{y}_{k,2}, \ldots, \mathbf{y}_{k,T}] \in \mathbb{C}^{M\times T}.$$

(3.3)

Then, define the vector $\mathbf{p} \triangleq \begin{bmatrix} p_1 & p_2 & \ldots & p_M \end{bmatrix}^T$ and apply wideband DFT to the stacked observation vector and calculate elements of $\mathbf{p} \in \mathbb{R}^{M\times 1}$ as follows

$$p_m = \sum_{k\in\mathcal{N}_c^{(\mathrm{s})}} \left\| [\mathbf{S}_k^H]_{(m,:)}\mathbf{Y}_k \right\|^2$$

(3.4)

Before proceeding further, let us present a lemma about asymptotic property of AoA steering matrix, say $\overline{\mathbf{U}}_k \triangleq [\overline{\mathbf{u}}_k(\theta_1)..\overline{\mathbf{u}}_k(\theta_L)] \in \mathbb{C}^{M\times L}$. This can help us to show how to pick AoA's by using the vector $\mathbf{p} \in \mathbb{R}^{M\times 1}$.

20

Lemma 1. *When $M \to \infty$, the wideband DFT response of $\overline{\boldsymbol{U}}_k$, is a tall sparse matrix with one nonzero element in each column, that is to say*

$$\lim_{M \to \infty} \left[\boldsymbol{S}_k^H \overline{\boldsymbol{U}}_k \right]_{n_l, l} \neq 0 \tag{3.5}$$

$\forall l, k$ and

$$n_l = \begin{cases} M\theta_\ell + 1 & \theta_\ell \in [0, \frac{d_{BS}}{\lambda_c}) \\ M + M\theta_\ell + 1 & \theta_\ell \in [-\frac{d_{BS}}{\lambda_c}, 0) \end{cases}. \tag{3.6}$$

Proof. See Appendix A. □

The lemma 1 provides two important insights. Firstly, it established that each unique θ value corresponds to different nonzero rows of the $\mathbf{S}_k^H \overline{\mathbf{U}}_k$ i.e. $n_\ell \neq n_i$ for any $\ell \neq i$ when d_{BS} is smaller or equal to $\lambda_c/2$ as is usually taken. Secondly, as $M \to \infty$, $\mathbf{S}_k^H \overline{\mathbf{U}}_k$ becomes row sparse matrix with full column rank. Hence, the wideband DFT response of the observation matrix, $\mathbf{S}_k^H \mathbf{Y}_k$ also exhibits row sparsity with the number of distinct AoA (i.e. L) nonzero rows. These all imply that the vector $\mathbf{p} \in \mathbb{R}^{M \times 1}$ becomes an asymptotic sparse vector with L non-zero elements when $M \to \infty$, each corresponding to one of the AoAs. Then we can easily estimate θ_ℓ values from the peak values of the vector $\mathbf{p} \in \mathbb{R}^{M \times 1}$.

However, M is finite in practice, resulting in a power leakage to nearby rows. This is known as the power leakage effect, which causes a mismatch between the discrete estimated angle and the real continuous angle [39–41]. To compensate for the power leakage, we apply an angle rotation operation as in [24] with the additional consideration of the beam-squint effect. The matrix that makes angle rotation is defined as

$$\boldsymbol{\Phi}_k(\Delta_\ell) = \mathrm{Diag}\left\{ 1, e^{i\Delta_\ell\left(1+\frac{f_k}{f_c}\right)}, \ldots, e^{i(M-1)\Delta_\ell\left(1+\frac{f_k}{f_c}\right)} \right\}. \tag{3.7}$$

Let $\widehat{L}$ denote the number of peaks in $\mathbf{p}$ and $\{m_\ell\}_{\ell=1}^{\widehat{L}}$ denote the corresponding row indexes of $\mathbf{p}$. Then, the optimal phase rotations $\{\Delta_\ell\}_{\ell=1}^{\widehat{L}}$ can be determined through

a one-dimensional search by addressing the the following problem:

$$\Delta_\ell = \operatorname*{argmax}_{\Delta\in[\frac{-\pi}{M}\frac{\pi}{M}]} \sum_{k=0}^{N_c-1} \left\| \left[\mathbf{S}_k^H\right]_{(m_\ell,:)} \mathbf{\Phi}_k^H(\Delta)\mathbf{Y}_k \right\|^2. \tag{3.8}$$

The BS-side AoA estimation procedure is summarized in Algorithm 1.

Algorithm 1 BS-side AoA Estimation

Input: $\mathbf{Y}_k$ in (3.3)

1: Calculate $p_m = \sum_{k\in\mathcal{N}_c^{(s)}} \left\| \left[\mathbf{S}_k^H\right]_{(m,:)} \mathbf{Y}_k \right\|^2 \ \forall m, \ \mathbf{p} = [p_1 \dots p_M]^T$

2: Find the row indexes of $\mathbf{p}$ with the power peak: $\{m_\ell\}_{\ell=1}^{\widehat{L}}$

3: Calculate the angle rotation parameters $\{\Delta_\ell\}_{\ell=1}^{\widehat{L}} \ \forall \ell = 1, \dots, \widehat{L}$:
$$\Delta_\ell = \operatorname*{argmax}_{\Delta\in[\frac{-\pi}{M}\frac{\pi}{M}]} \sum_{k\in\mathcal{N}_c^{(s)}} \left\| \left[\mathbf{S}_k^H\right]_{(m_\ell,:)} \mathbf{\Phi}_k^H(\Delta)\mathbf{Y}_k \right\|^2,$$
where $\mathbf{\Phi}_k(\Delta_\ell) \triangleq \operatorname{Diag}\left\{1, e^{i\Delta_\ell\left(1+\frac{f_k}{f_c}\right)}, \dots, e^{i(M-1)\Delta_\ell\left(1+\frac{f_k}{f_c}\right)}\right\}$

4: Estimate AoAs for $1 \le \ell \le \widehat{L}$:
$$\widehat{\theta}_\ell = \begin{cases} \arcsin\left(\frac{\lambda_c(m_\ell-1)}{d_{\text{BS}}M} - \frac{\lambda_c\Delta_\ell}{2\pi d_{\text{BS}}}\right) & m_\ell \le M\frac{d_{\text{BS}}}{\lambda_c} \\[2ex] \arcsin\left(\frac{\lambda_c(m_\ell-M-1)}{d_{\text{BS}}M} - \frac{\lambda_c\Delta_\ell}{2\pi d_{\text{BS}}}\right) & m_\ell > M\frac{d_{\text{BS}}}{\lambda_c} \end{cases}$$

Output: Estimates of the BS-side AoAs: $\left\{\widehat{\theta}_\ell\right\}_{\ell=1}^{\widehat{L}}$

3.2 Cascaded Angle-Delay Estimation

In the ST-PE mode, once the AoAs are estimated at the BS, the focus shifts to de-couple these angles from the acquired signal. Then the next step is to estimate the cascaded angle and delay parameters. For this estimation purpose, we utilize beam-squint aware joint OMP whose implementation is efficient. Let us re-express the received signal $\mathbf{y}_{k,n}$ in (3.1) in matrix-vector form as

$$\mathbf{y}_{k,n} = \overline{\mathbf{U}}_k \begin{bmatrix} y_{1,k,n} & y_{2,k,n} & \dots & y_{L,k,n} \end{bmatrix}^T + \mathbf{n}_{k,n}, \tag{3.9}$$

where $\overline{\mathbf{U}}_k$ is the previously defined AoA steering matrix and $y_{\ell,k,n}$ can be defined in terms of cascaded angle and delay as follows

$$y_{\ell,k,n} \triangleq \sum_{j=1}^{J} \gamma_{\ell,j,n} e^{-i2\pi(f_k+f_c)\tau_{\ell,j}} \left[\boldsymbol{\phi}_n^T \mathbf{u}_k(\varrho_{\ell,j}) \right]. \tag{3.10}$$

If we gather cascaded angle and delay, and define $d_{k,n}(\varrho, \tau) \triangleq e^{-i2\pi(f_k+f_c)\tau} \left[(\boldsymbol{\phi}_n^{(\mathrm{s})})^T \mathbf{u}_k(\varrho) \right]$, then equation 3.10 can be written in a more compact way as

$$y_{\ell,k,n} \triangleq \sum_{j=1}^{J} \gamma_{\ell,j,n} d_{k,n}(\varrho_{\ell,j}, \tau_{\ell,j}) \tag{3.11}$$

With the estimated AoAs $\{\widehat{\theta}_\ell\}_{\ell=1}^{\widehat{L}}$, we can construct estimated steering matrix i.e. $\widehat{\overline{\mathbf{U}}}_k \triangleq \left[\overline{\mathbf{u}}_k(\widehat{\theta}_1) \quad \overline{\mathbf{u}}_k(\widehat{\theta}_2) \quad \ldots \quad \overline{\mathbf{u}}_k(\widehat{\theta}_L) \right]$. Then, based on the $\widehat{\overline{\mathbf{U}}}_k^\dagger \overline{\mathbf{U}}_k \approx \mathbf{I}_L$ where $\widehat{\overline{\mathbf{U}}}_k^\dagger \triangleq (\widehat{\overline{\mathbf{U}}}_k^H \widehat{\overline{\mathbf{U}}}_k)^{-1} \widehat{\overline{\mathbf{U}}}_k^H$, we can project the received signal onto the subspace formed by the AoA steering matrix. This projection helps in decoupling the effects of AoAs from the received signal and can be performed as follows

$$\widetilde{\mathbf{y}}_{k,n} \triangleq \widehat{\overline{\mathbf{U}}}_k^\dagger \mathbf{y}_{k,n} \approx \left[y_{1,k,n} \quad y_{2,k,n} \quad \ldots \quad y_{L,k,n} \right]^T + \widehat{\overline{\mathbf{U}}}_k^\dagger \mathbf{n}_{k,n}. \tag{3.12}$$

Let us focus the ℓth element of the projected received signal $\widetilde{\mathbf{y}}_{k,n}$ and concatenate it over $\forall k \in \mathcal{N}_c^{(\mathrm{s})}$ to obtain the following:

$$\mathbf{z}_{\ell,n} \triangleq \left[y_{\ell,1,n} \quad \ldots \quad y_{\ell,N_c,n} \right]^T + \widetilde{\mathbf{n}}_{\ell,n} \in \mathbb{C}^{N_c^{(\mathrm{s})} \times 1}, \tag{3.13}$$

where $\widetilde{\mathbf{n}}_{\ell,n} \triangleq \left[\widetilde{n}_{\ell,1,n} \quad \ldots \quad \widetilde{n}_{\ell,N_c,n} \right]^T$ is the resultant noise on the ℓth MPC and its elements can be expressed as $\widetilde{n}_{\ell,k,n} \triangleq [\widehat{\overline{\mathbf{U}}}_k^\dagger \mathbf{n}_{k,n}]_{(\ell)}$.

Furthermore, let us concatenate $d_{k,n}(\varrho, \tau)$'s over $\forall k \in \mathcal{N}_c^{(\mathrm{s})}$ and define $\mathbf{d}_n(\varrho, \tau) \triangleq \left[d_{1,n}(\varrho, \tau) \quad \ldots \quad d_{N_c,n}(\varrho, \tau) \right]^T \in \mathbb{C}^{N_c^{(\mathrm{s})} \times 1}$. Then, the vector $\mathbf{z}_{\ell,n}$ in (3.13) can be expressed in matrix-vector form as

$$\mathbf{z}_{\ell,n} = \left[\mathbf{d}_n(\varrho_{\ell,1}, \tau_{\ell,1}) \quad \ldots \quad \mathbf{d}_n(\varrho_{\ell,J}, \tau_{\ell,J}) \right] \begin{bmatrix} \gamma_{\ell,1,n} \\ \vdots \\ \gamma_{\ell,J,n} \end{bmatrix} + \widetilde{\mathbf{n}}_{\ell,n}. \tag{3.14}$$

Note that ℓ^{th} path cascaded directional sines $\varrho_{\ell,j}$ and delays $\tau_{\ell,j}$ can be extracted using the concatenated matrix of $\mathbf{z}_{\ell,n}$. For this purpose, (3.14) can be approximated by applying the virtual angular domain (VAD) representation as

$$\mathbf{z}_{\ell,n} = \mathbf{D}_n \mathbf{b}_n + \widetilde{\mathbf{n}}_{\ell,n}, \tag{3.15}$$

where $\mathbf{D}_n \in \mathbb{C}^{N_c^{(s)} \times N_\varrho N_\tau}$ is an overcomplete dictionary matrix whose columns are the possible steering vector of the cascaded sines. N_ϱ and N_τ are the number of grid points for the cascaded angle, and the number of grid points for cascaded delay respectively. The dictionary grids can be obtained by uniform division of the possible intervals as follows

$$\mathcal{S}_{\widetilde{\varrho}} \triangleq \left\{ \widetilde{\varrho}_i \triangleq -2 + (i-1)\frac{4}{N_\varrho - 1}, \ \forall i = 1, 2, \ldots, N_\varrho \right\}, \tag{3.16}$$

$$\mathcal{S}_{\widetilde{\tau}} \triangleq \left\{ \widetilde{\tau}_i \triangleq (i-1)\frac{\widetilde{\tau}_{\max}}{N_\tau - 1}, \ \forall i = 1, 2, \ldots, N_\tau \right\}, \tag{3.17}$$

where $\widetilde{\tau}_{\max} \triangleq \overline{\tau}_{\max} + \tau_{\max}$ represents the maximum cascaded delay. Then, the dictionary matrix $\mathbf{D}_n$ can be constructed as

$$\mathbf{D}_n = \mathbf{d}_n(\mathcal{S}_{\widetilde{\varrho}} \times \mathcal{S}_{\widetilde{\tau}}) \triangleq \left[\mathbf{d}_n(\widetilde{\varrho}_1, \widetilde{\tau}_1) \ \ldots \ \mathbf{d}_n(\widetilde{\varrho}_{N_\varrho}, \widetilde{\tau}_{N_\tau}) \right]. \tag{3.18}$$

Recall that $\mathbf{b}_n \in \mathbb{C}^{N_\varrho N_\tau \times 1}$ in (3.15) is a sparse vector in angular domain with J cascaded gains as nonzero elements. Therefore, we approach the cascaded angle-delay pairs extraction as a sparse signal recovery problem and propose a BSA OMP algorithm to solve this problem. The proposed implementation of the OMP algorithm also introduces an efficient approach. In the OMP algorithm, as the grid size increases, it divides the interval into smaller segments, enabling a higher-resolution search that yields improved performance. However, increasing the grid size comes with a complexity trade-off. Therefore, the proposed OMP method initially divides the possible interval into fewer grids in a uniform manner, leading to a coarse estimation based on this grid partitioning. Subsequently, it refines the dictionary around the estimated

coarse angles and delays, using a limited number of grids again. This refined process enables a more precise search with fewer grids. With each iteration, the estimated angle-delay pairs are updated, and this procedure is repeated, ultimately resulting in more accurate estimations. One more important point is that appropriate RIS phase shift design is crucial for OMP performances and will be explained in the last section of this chapter. Finally, it should be noted that OMP processes its observations either coherently or non-coherently, depending on the level of correlation it encounters. In non-coherent mode, if it chooses to operate as such, it calculates the final correlations by summing the magnitudes of the correlations obtained at different time instances while discarding their phases. Coherent mode, on the other hand, combines both magnitudes and phases of the correlations. OMP can decide which mode to operate in over time. It may initially run in non-coherent mode. Later, if the gains it obtains become correlated with each other, it can switch to coherent mode to avoid any loss in the observations it receives. The proposed BSA efficient OMP algorithm is summarized in algorithm 2.

3.3   Angle-Delay Scaling Property

As previously explained, the OMP algorithm is employed for a specific MPC between BS and RIS with the goal of identifying J cascaded angle-delay pairs. Given that there are L such MPCs between BS and RIS, executing OMP L times becomes necessary to find all these pairs. This would result in a total of JL parameter estimations. Nevertheless, this circumstance implies that overall computational complexity for the estimation of cascaded parameter scales with L. On the other hand, we know that linear correlation exists among the resulting JL cascaded paths due to the common paths formed between UE and RIS as stated in [24]. In more detail, there is angle and delay scaling between cascaded multipaths formed by different AoDs from the RIS. This scaling property suggests an alternative approach: rather than directly estimating JL cascaded angle-delay pairs, we can conduct the OMP algorithm for J parameters and subsequently deduce L scalings. This strategy enables us to estimate a total of $J + L$ parameters which delivers a notable advantage in terms of complexity. This concept can be referred to as *angle-delay scaling property (ADSP)* and inspired

Algorithm 2 Joint OMP for Cascaded Angle-Delay Estimation

Input: $\mathbf{z}_{\ell,n} \ \forall n \in \{1, 2, \ldots, T\}$ in (3.13)

1: Set the number of cascaded angle and delay grids: N_ϱ, N_τ

2: Construct the angle and delay grids:
$$\mathcal{S}_{\widetilde{\varrho}}^{(0)} \triangleq \left\{ \widetilde{\varrho}_i \triangleq -2 + (i-1)\frac{4}{N_\varrho - 1}, \quad \forall i = 1, 2, \ldots, N_\varrho \right\},$$
$$\mathcal{S}_{\widetilde{\tau}}^{(0)} \triangleq \left\{ \widetilde{\tau}_i \triangleq (i-1)\frac{\overline{\tau}_{\max} + \tau_{\max}}{N_\tau - 1}, \quad \forall i = 1, 2, \ldots, N_\tau \right\}.$$

3: Construct the dictionary $\mathbf{D}_n^{(0)} \ \forall n$:
$$\mathbf{D}_n^{(0)} = \mathbf{d}_n(\mathcal{S}_{\widetilde{\varrho}} \times \mathcal{S}_{\widetilde{\tau}}) \triangleq \begin{bmatrix} \mathbf{d}_n(\widetilde{\varrho}_1, \widetilde{\tau}_1) & \ldots & \mathbf{d}_n(\widetilde{\varrho}_{N_\varrho}, \widetilde{\tau}_{N_\tau}) \end{bmatrix}$$

4: Set: $\mathbf{r}_n = \mathbf{z}_{\ell,n} \ \forall n$, $\mathbf{Z}_n = [\ ] \ \forall n$, $i = 0$

5: **while** $\sum_{n=1}^{T} \|\mathbf{r}_n\|^2 > $ threshold **do**

6:     $i = i + 1$

7:     $\mathbf{D}_n = \mathbf{D}_n^{(0)} \in \mathbb{C}^{N_c \times N_\varrho N_\tau} \ \forall n$ # Coarse dictionary

8:     **for** $j = 1$ **to** N_{iter} **do**

9:         $\mathbf{p} = \sum_{n=1}^{T} |\mathbf{D}_n^H \mathbf{r}_n|$ # Sum correlation vector over all times

10:         Find $(\widehat{\varrho}_{\ell,i}, \widehat{\tau}_{\ell,i})$ that corresponds to the maximum index of $\mathbf{p}$

           # Narrow the dictionary around $(\widehat{\varrho}_{\ell,i}, \widehat{\tau}_{\ell,i})$:

11:         $\Delta_{\widetilde{\varrho}} = \Delta_{\widetilde{\varrho}}/2^j, \Delta_{\widetilde{\tau}} = \Delta_{\widetilde{\tau}}/2^j$ # Grid refinement parameters

12:         $\mathcal{S}_{\widetilde{\varrho}}^{(j)} = \text{linspace}\left(\widehat{\varrho}_{\ell,i} - \Delta_{\widetilde{\varrho}}, \widehat{\varrho}_{\ell,i} + \Delta_{\widetilde{\varrho}}, N_\varrho\right)$ # Refined angle grid

13:         $\mathcal{S}_{\widetilde{\tau}}^{(j)} = \text{linspace}\left(\widehat{\tau}_{\ell,i} - \Delta_{\widetilde{\tau}}, \widehat{\tau}_{\ell,i} + \Delta_{\widetilde{\tau}}, N_\tau\right)$ # Refined delay grid

14:         $\mathbf{D}_n = \mathbf{d}_n(\mathcal{S}_{\widetilde{\varrho}}^{(j)} \times \mathcal{S}_{\widetilde{\tau}}^{(j)}) \in \mathbb{C}^{N_c \times N_\varrho N_\tau} \ \forall n$ # Refined dictionary

15:         $\mathbf{D}_n = \text{vecnorm}\{\mathbf{D}_n\}$ # Normalize the dictionary

16:     **end for**

17:     $\mathbf{Z}_n = \begin{bmatrix} \mathbf{Z}_n & \mathbf{d}_n(\widehat{\varrho}_{\ell,i}, \widehat{\tau}_{\ell,i}) \end{bmatrix} \in \mathbb{C}^{N_c \times i} \ \forall n$ # Update the basis

18:     $\mathbf{r}_n = \mathbf{z}_{\ell,n} - \mathbf{Z}_n \mathbf{Z}_n^{\dagger} \mathbf{z}_{\ell,n} \ \forall n$ # Update the residual

19: **end while**

Output: $\widehat{J} = i$ and $\{(\widehat{\varrho}_{\ell,j}, \widehat{\tau}_{\ell,j})\}_{j=1}^{\widehat{J}}$

by the study [24]. Let us write the expression of the lth path received signal projected onto AoA subspace from the equation (3.12) as follows

$$\widetilde{y}_{\ell,k,n} = \sum_{j=1}^{J} \gamma_{\ell,j,n} \boldsymbol{\phi}_n^T \mathbf{g}_{k,\ell,j} + \widetilde{n}_{\ell,k,n} \tag{3.19}$$

where $\mathbf{g}_{k,\ell,j} \in \mathbb{C}^{N\times 1}$ is purely composed of cascaded angle and delay pairs and can be defined as $\mathbf{g}_{k,\ell,j} \triangleq e^{-i2x(f_{k+1}f_c)\tau_{\ell,j}} \mathbf{u}_k(\varrho_{\ell,j})$. Then (3.19) equation can be written for r^{th} path as follows

$$\widetilde{y}_{r,k,n} = \sum_{j=1}^{J} \gamma_{r,j,n} \boldsymbol{\phi}_n^T \mathbf{g}_{k,r,j} + \widetilde{n}_{r,k,n} \tag{3.20}$$

Here, it is proposed that $\mathbf{g}_{k,r,j}$ can be expressed in terms of $\mathbf{g}_{k,\ell,j}$ due to angle-delay scaling property

$$\begin{aligned}
\mathbf{g}_{k,r,j} &= e^{-i2\pi(f_k+f_c)(\overline{\tau}_r+\tau_j)} \mathbf{u}_k(\vartheta_j - \varphi_\ell) \\
&= e^{-i2\pi(f_k+f_c)(\overline{\tau}_l+\tau_j)} e^{-i2\pi(f_k+f_c)(\overline{\tau}_r-\overline{\tau}_l)} \operatorname{diag}(\mathbf{u}_k(\varphi_\ell - \varphi_r)) \mathbf{u}_k(\vartheta_j - \varphi_\ell) \quad (3.21) \\
&= e^{-i2\pi(f_k+f_c)(\Delta\tau_r)} \operatorname{diag}(\mathbf{u}_k(\Delta\varphi_r)) \mathbf{g}_{k,\ell,j}
\end{aligned}$$

where $\Delta\varphi_r \triangleq \varphi_l - \varphi_r$, $\Delta\tau_r \triangleq \overline{\tau}_r - \overline{\tau}_l$ and they can be called r path angle and delay scalings respectively. Let us plug equation (3.21) into (3.20) and write projected received signal on the rth path by using the angle-delay pairs of the lth path as

$$\widetilde{y}_{r,k,n} = \boldsymbol{\phi}_n^T e^{-i2\pi(f_k+f_c)\Delta\tau_r} \operatorname{diag}(\mathbf{u}_k(\Delta\varphi_r)) \sum_{j=1}^{J} \gamma_{r,j,n} \mathbf{g}_{k,\ell,j} + \widetilde{n}_{r,k,n} \tag{3.22}$$

In order to express equation (3.22) in a matrix form, concatenate $\mathbf{g}_{k,\ell,j}$ along the UE-RIS paths as $\mathbf{G}_{k,\ell} \triangleq [\mathbf{g}_{k,\ell,1} \ldots \mathbf{g}_{k,\ell,J}] \in C^{N\times J}$ and $\gamma_{r,j,n}$ as $\boldsymbol{\gamma}_{r,n} \triangleq [\gamma_{r,1,n} \ldots \gamma_{r,J,n}] \in C^{J\times 1}$, then re-write the equation (3.22) as

$$\widetilde{y}_{r,k,n} = \boldsymbol{\phi}_n^T e^{-i2\pi(f_k+f_c)\Delta\tau_r} \operatorname{diag}(\mathbf{u}_k(\Delta\varphi_r)) \mathbf{G}_{k,\ell} \boldsymbol{\gamma}_{r,n} + \widetilde{n}_{r,k,n} \tag{3.23}$$

To find a cascaded angle-delay pair for the rth path, we need to estimate scalings i.e. $\Delta\tau_r$ and $\Delta\varphi_r$. Therefore bring these unknowns together and define the following

$$\mathbf{z}_{n,k,r}(\Delta\varphi_r, \Delta\tau_r) \triangleq \boldsymbol{\phi}_n^T e^{-i2\pi(f_k+f_c)\Delta\tau_r} \operatorname{diag}(\mathbf{u}_k(\Delta\varphi_r))\mathbf{G}_{k,\ell} \in C^{1\times J} \tag{3.24}$$

Remember that we do not pay attention to cascaded gain estimation at this moment, and our aim is to identify slowly varying parameters in this mode. Therefore we do not include $\boldsymbol{\gamma}_{r,n}$ into the expression in (3.24). Let us continue by concatenating observations given in (3.20) along both the time and frequency indices and get

$$\begin{aligned}
\widetilde{\mathbf{y}}_r &= [\widetilde{y}_{1,1,r} \ldots \widetilde{y}_{1,N_c,r}, \widetilde{y}_{2,1,r}, \ldots \widetilde{y}_{T,N_c,r}]^T \\
&= \operatorname{blkdiag}\{\mathbf{Z}_{n,r}\}_{n=1}^T [\boldsymbol{\gamma}_{r,1} \ldots \boldsymbol{\gamma}_{r,T}]^T + \widetilde{n}_r
\end{aligned} \tag{3.25}$$

where $\mathbf{Z}_{n,r} \in \mathbb{C}^{N_c^{(s)}\times J}$ is the stack of $\mathbf{z}_{n,k,r}$, which can be represented as $\mathbf{Z}_{n,r} \triangleq [\mathbf{z}_{n,1,r} \ldots \mathbf{z}_{n,N_c,r}]^T$ and $\widetilde{n}_r \in \mathbb{C}^{N_c^{(s)}T\times 1}$ is the resultant noise whose definition can be given as $\widetilde{n}_r \triangleq [\widetilde{n}_{1,1,r} \ldots \widetilde{n}_{1,N_c,r}, \widetilde{n}_{2,1,r}, \ldots \widetilde{n}_{T,N_c,r}]^T$. For the sake of clarity, further definitions can be made such that $\mathbf{Z}_r(\Delta\varphi_r, \Delta\tau_r) \triangleq \operatorname{blkdiag}\{\mathbf{Z}_{n,r}\}_{n=1}^T \in \mathbb{C}^{N_c^{(s)}T\times JT}$ and $\boldsymbol{\gamma}_r \triangleq [\boldsymbol{\gamma}_{r,1}, \ldots \boldsymbol{\gamma}_{r,T}]^T \in \mathbb{C}^{JT\times 1}$, then concatenated observations can be stated in a more clear way as

$$\widetilde{\mathbf{y}}_r = \mathbf{Z}_r(\Delta\varphi_r, \Delta\tau_r)\boldsymbol{\gamma}_r + \widetilde{n}_r \tag{3.26}$$

The estimation of delay and angle scalings constitutes a non-random multi-parameter estimation problem onto the equation (3.26). As described in [42], this problem can be modeled as a separable gaussian model and its maximum likelihood (ML) solution can be given by using the projection matrix as

$$\Delta\widehat{\varphi}_r, \Delta\widehat{\tau}_r = \arg\max_{\Delta\varphi_r, \Delta\tau_r} \|\mathbf{P}_{\mathbf{Z}_r}(\Delta\varphi_r, \Delta\tau_r)\widetilde{\mathbf{y}}_r\| \tag{3.27}$$

where $\mathbf{P}_{\mathbf{Z}_r}(\Delta\varphi_r, \Delta\tau_r)$ represents complex projection matrix defined on $\mathbf{Z}_r(\Delta\varphi_r, \Delta\tau_r)$ as $\mathbf{P}_{\mathbf{Z}_r}(\Delta\varphi_r, \Delta\tau_r) \triangleq \mathbf{Z}_r(\Delta\varphi_r, \Delta\tau_r)(\mathbf{Z}_r(\Delta\varphi_r, \Delta\tau_r)\mathbf{Z}_r(\Delta\varphi_r, \Delta\tau_r)^H)^{-1}\mathbf{Z}_r(\Delta\varphi_r, \Delta\tau_r)^H$.

After finding angle-delay pair scalings, cascaded parameters of the rth can be immediately found by using the outputs of the previously launched OMP as follows

$$\varrho_{r,j} = \vartheta_j - \varphi_\ell + \varphi_\ell - \varphi_r = \varrho_{\ell,j} + \Delta\varphi_r \quad \forall j \in \{1,\ldots,J\} \qquad (3.28)$$

$$\tau_{r,j} = \bar{\tau}_\ell + \tau_j + \bar{\tau}_r - \bar{\tau}_\ell = \tau_{\ell,j} + \Delta\tau_r \quad \forall j \in \{1,\ldots,J\} \qquad (3.29)$$

Finally, the efficiency of the angle-delay scaling property is worth highlighting. Despite involving a search for estimating the scalings, it remains more efficient compared to the individual execution of OMP, where the latter requires conducting a disjoint search J times for each path between the BS and RIS.

3.4   RIS Phase Shift Design

In the communication link involving the RIS, BS, and UE, the composite channel experienced between them heavily relies on the RIS phase shift, as evident from the equation (2.2) where the channel matrix is a function of the RIS phase shift design. Therefore, the RIS phase shift design not only impacts the channel itself but also influences the performance of the method employed for channel estimation. In an extreme scenario, let's consider that the RIS reflects incoming signals in a direction different from the BS. In this case, no signal information would be obtained at the BS, making channel estimation impossible. Thus, the channel estimation problem in RIS-aided systems is considered as two separate operations: the channel estimation itself and the RIS phase shift design given its interdependence. Within the ST-PE mode, RIS design is tailored to the objectives for these reasons. In this mode, the BS lacks knowledge of the channel and needs to gather information by exploring potential regions. As a result, the intended sector is divided into T sub-angular regions. Similar to previous studies [43], [20], [19], the DFT matrix is used as the RIS phase shift matrix, with each region is targeted by DFT columns corresponding to the target sub-region. This approach ensures that the RIS design is in line with the goals of the ST-PE mode. Moreover, the practical challenges of amplitude-phase coupling

explained in section 2.3 are addressed in RIS design. This leads us to adopt a more realistic design approach. Let us first express phase shifts of the ideal RIS from the DFT matrix as

$$\phi_{m,n} = e^{-1i\frac{2\pi}{M}(m-1)(n-1)} \quad \forall m \in \{1,\ldots,M\}, \forall n \in \{1,\ldots,T\} \tag{3.30}$$

Note that the amplitude of the RIS element given in the equation (3.30) is unity which is non-realistic explained previously. Then to make it realistic, let us plug the equation in (2.9) into the (3.30) as

$$\phi_{m,n} = ((1-\beta_{\min})\left(\frac{\sin\left(\angle e^{-1i\frac{2\pi}{M}(m-1)(n-1)} - \phi_0\right) + 1}{2}\right)^{a_0} + \beta_{\min})e^{-1i\frac{2\pi}{M}(m-1)(n-1)} \tag{3.31}$$

The resulting beampatterns of both ideal and practical RIS phase shift design using the DFT matrix when T is equal to the N are depicted in figure 3.1. It is important to observe that the power level of the practical RIS design is lower compared to the ideal one, attributed to the power loss experienced by the RIS in real-world scenarios.

In the initial coherence blocks when the system starts, no angle and delay information of the channel is available. Hence, during these periods, it is necessary to keep the intended sector-wide to estimate the channel effectively. To achieve this, more OFDM symbols can be utilized along with a broader beam coverage to scan the larger area. That means it makes a full scan and the region that is directed by RIS beams can be seen in figure 3.2. However, maintaining such a wide sector becomes unnecessary in the following coherence blocks. The system already possesses the angle and delay information estimated before its operation, and these parameters tend to change gradually. Therefore, with an awareness of this change, a tracking logic can be employed to scan only around those angles, adopting a sort of tracking mechanism. This approach significantly reduces the required time for the ST-PE mode and can be referred to as a partial scan whose sample targeted region can be seen in the same figure 3.2. Nevertheless, it's worth noting that this aspect hasn't been addressed in current implementations and could be a starting point for further research in subsequent stud-
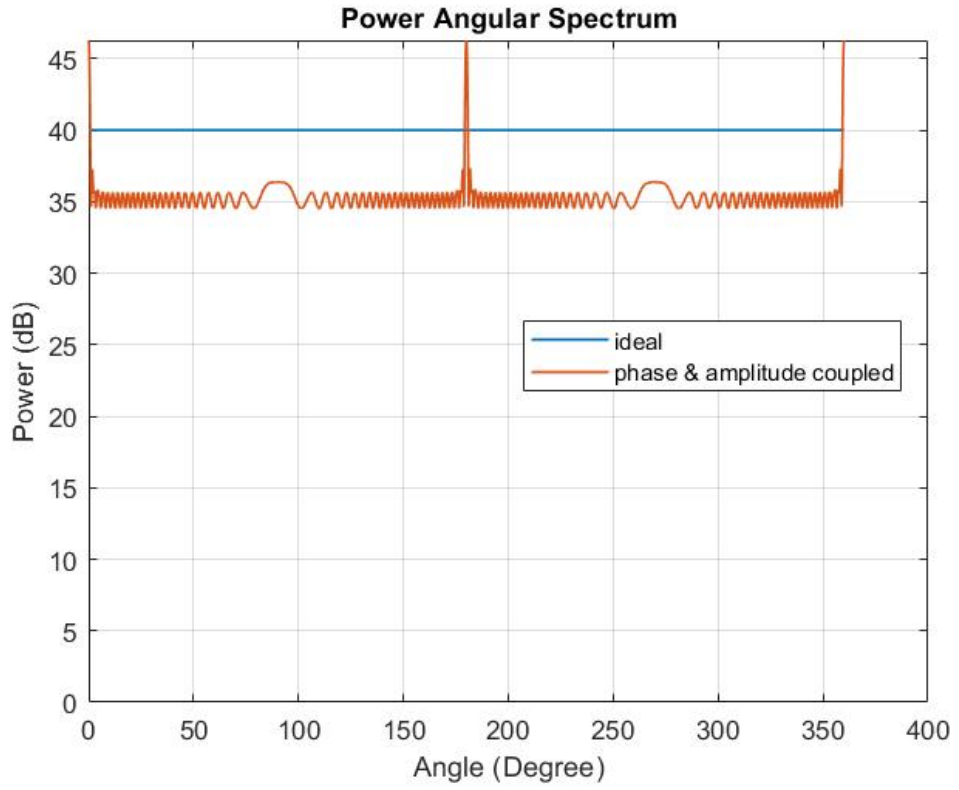
Figure 3.1: Power angular spectrum of the RIS phase shift design in ST-PE mode
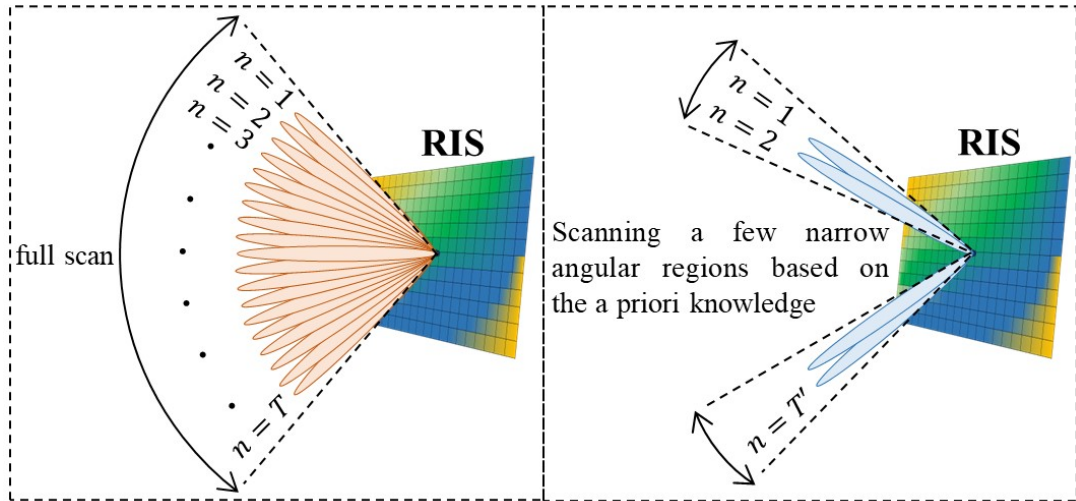
ies.

Figure 3.2: RIS beam scanning regions

CHAPTER 4

FAST-TIME PARAMETER ESTIMATION

Once the estimates of the slowly varying angles and delays are obtained within the ST-PE mode, the user's primary goal is to facilitate effective communication based on this information. Due to rapid change in channel gains as mentioned earlier, the user needs to estimate these gains at the same time. Therefore, while allocating its main resources for communication, the user also dedicates limited resources to running the FT-PE mode. During this mode, the user starts by formulating the channel gain estimation using the acquired delay and angle information and attempts to estimate gains in a cascaded form at the BS using a well-known method like the LS method. Furthermore, using the prior estimated parameters, the user refines the RIS design, denoted by $\boldsymbol{\phi}^{(\mathrm{f})}$ and effectively reflects UE signals to the BS side. This refined design remains in use throughout the whole FT-PE mode and boosts the communication performance. In this mode, the user transmits pilot symbol sequences over a selected subset of subcarriers, denoted by $\mathcal{N}_c^{(\mathrm{f})}$ subcarriers out of the total N_c. Notably, the rapidly changing channel gains are independently estimated for each time instance.

Let $\mathcal{N}_c^{(\mathrm{f})} \triangleq \left\{ 1, \frac{N_c}{N_c^{(\mathrm{f})}-1}, \frac{2N_c}{N_c^{(\mathrm{f})}-1}, \frac{3N_c}{N_c^{(\mathrm{f})}-1}, \ldots, N_c \right\}$ denote the indexes of the subcarriers allocated for the FT-PE such that $|\mathcal{N}_c^{(\mathrm{f})}| = N_c^{(\mathrm{f})}$. Since the BS has knowledge of the pilot sequences, we can make the assumption that $x_{k,n} = 1 \; \forall k \in \mathcal{N}_c^{(\mathrm{f})}, \forall n$ during the FT-PE mode without losing generality. In this way, we can eliminate the information symbol $x_{k,n}$ in (2.1). Then the received signal $\mathbf{y}_{k,n}$ within the FT-PE mode can be expressed for the kth subcarrier at the nth time instance using (3.1) as

$$\mathbf{y}_{k,n} = \mathbf{g}_{k,n} + \mathbf{n}_{k,n} \triangleq \sum_{\ell=1}^{L} \sum_{j=1}^{J} \gamma_{\ell,j,n} \alpha_{\ell,j,k} \overline{\mathbf{u}}_k(\theta_\ell) + \mathbf{n}_{k,n}, \qquad (4.1)$$

33

where $\mathbf{g}_{k,n} \in \mathbb{C}^{M \times 1}$ represents the composite channel between the BS and the UE, while the scalar $\alpha_{\ell,j,k}$ is constructed from the previously derived cascaded parameters along with the RIS phase shift utilized within this mode. This scalar can be defined as $\alpha_{\ell,j,k} \triangleq e^{-i2\pi(f_k+f_c)\tau_{\ell,j}}[(\boldsymbol{\phi}^{(\mathrm{f})})^T \mathbf{u}_k(\varrho_{\ell,j})]$.

4.1 Cascaded Gain Estimation

In the context of the FT-PE mode, the conducted channel estimation involves the estimation of cascaded gains $\gamma_{\ell,j,n}$. This process begins with the reconfiguration of the channel description from the perspective of the BS and continues further with the employment of the LS method. The subsequent step involves the restructuring of the channel to make it representable as a vector within the subspace spanned by the gradually changing channel parameters. As an income of this transformation, the received signal should be converted into a matrix-vector multiplication format. To facilitate this transformation, we introduce the subsequent definitions.

$$\boldsymbol{\alpha}_k \triangleq \left[[\alpha_{1,1,k}, \ \ldots \ , \alpha_{1,J,k}], \ \ldots \ , [\alpha_{L,1,k}, \ \ldots \ , \alpha_{L,J,k}] \right]^T_{LJ \times 1}, \tag{4.2}$$

$$\boldsymbol{\gamma}_n \triangleq \left[[\gamma_{1,1,n}, \ \ldots \ , \gamma_{1,J,n}], \ \ldots \ , [\gamma_{L,1,n}, \ \ldots \ , \gamma_{L,J,n}] \right]^T_{LJ \times 1}. \tag{4.3}$$

Here, the terms $\boldsymbol{\alpha}_k$ and $\boldsymbol{\gamma}_n$ are essentially the vectorized forms of the $\alpha_{\ell,j,k}$ and channel gains $\gamma_{\ell,j,k}$ defined for all cascaded MPCs formed between the UE and BS. Then, the received signal in (4.1) can be expressed using these definitions as

$$\mathbf{y}_{k,n} = \left(\overline{\mathbf{U}}_k \otimes \mathbf{1}_{1 \times J} \right) \mathrm{diag}(\boldsymbol{\alpha}_k) \boldsymbol{\gamma}_n + \mathbf{n}_{k,n}, \tag{4.4}$$

To enhance the clarity and compactness of the given expression, we can take one more step in simplification. For this purpose, we can introduce a matrix $\mathbf{W}_k^{(\mathrm{f})} \in \mathbb{C}^{M \times LJ}$, defined as $\mathbf{W}_k^{(\mathrm{f})} \triangleq \left(\overline{\mathbf{U}}_k \otimes \mathbf{1}_{1 \times J} \right) \mathrm{diag}(\boldsymbol{\alpha}_k)$. With this definition, the received signal obtained at the kth subcarrier and n^{th} time instance in matrix-vector multiplication form can be expressed in the final version as follows

$$\mathbf{y}_{k,n} = \mathbf{W}_k^{(f)} \boldsymbol{\gamma}_n + \mathbf{n}_{k,n}, \qquad (4.5)$$

The observations required for gain estimation can be obtained by concatenating the received signals over the subcarriers. This concatenation process yields the resulting $\mathbf{y}_n \triangleq \begin{bmatrix} \mathbf{y}_{1,n}^T & \mathbf{y}_{2,n}^T & \cdots & \mathbf{y}_{N_c^{(f)},n}^T \end{bmatrix}^T \in \mathbb{C}^{MN_c^{(f)} \times 1}$ which can be expressed as follows

$$\mathbf{y}_n = \mathbf{g}_n + \mathbf{n}_n = \mathbf{W}^{(f)} \boldsymbol{\gamma}_n + \mathbf{n}_n, \qquad (4.6)$$

where $\mathbf{W}^{(f)}$ is obtained by combining $\mathbf{W}_k^{(f)}$ across the subcarriers in a similar manner i.e. $\mathbf{W}^{(f)} \triangleq \begin{bmatrix} (\mathbf{W}_1^{(f)})^T & (\mathbf{W}_2^{(f)})^T & \cdots & (\mathbf{W}_{N_c^{(f)}}^{(f)})^T \end{bmatrix}^T \in \mathbb{C}^{MN_c^{(f)} \times LJ}$. It's important to note that this matrix can be constructed in this mode as $\widehat{\mathbf{W}}^{(f)}$ due to its dependence on the slowly varying parameters and RIS phase shifts. Leveraging the estimated cascaded delay and angle parameters from the ST-PE mode, first we can reconstruct the $\alpha_{\ell,j,k}$ as $\widehat{\alpha}_{\ell,j,k} = e^{-i2\pi(f_k + f_c)\widehat{\tau}_{\ell,j}} [(\boldsymbol{\phi}^{(f)})^T \mathbf{u}_k(\widehat{\varrho}_{\ell,j})]$ and then derive the BS-Side AoA steering matrix $\mathbf{U}_k$ via $\widehat{\overline{\mathbf{U}}}_k \triangleq \begin{bmatrix} \overline{\mathbf{u}}_k(\widehat{\theta}_1) & \overline{\mathbf{u}}_k(\widehat{\theta}_2) & \cdots & \overline{\mathbf{u}}_k(\widehat{\theta}_L) \end{bmatrix}$ as we did previously. At the end of these steps, we can rewrite $\mathbf{y}_n$ in (4.6) using the constructed as

$$\mathbf{y}_n = \mathbf{g}_n + \mathbf{n}_n \approx \widehat{\mathbf{W}}^{(f)} \boldsymbol{\gamma}_n + \mathbf{n}_n. \qquad (4.7)$$

In the equation 4.7, the only remaining unknown parameter aside from the noise terms is $\boldsymbol{\gamma}_n$. Then, using the LS solution for $\breve{\boldsymbol{\gamma}}_n$, we estimate the channel gains as

$$\widehat{\breve{\boldsymbol{\gamma}}}_n = [\widehat{\mathbf{W}}^{(f)}]^\dagger \mathbf{y}_n. \qquad (4.8)$$

In constructing $\widehat{\mathbf{W}}^{(f)}$, we adopt a unique approach that does not directly use the estimated slowly varying parameters. Instead, we treat the parameter sets $\breve{\mathcal{S}}_\theta$ and $\breve{\mathcal{S}}_{\varrho_\ell,\tau_\ell}$ as if they were the AoA at the BS and the cascaded angle-delay pairs estimation, respectively. The set $\breve{\mathcal{S}}_\theta \triangleq \{\hat{\theta}_\ell \pm \Delta_\theta\}_{\ell=1}^{\widehat{L}}$ consists of $\hat{\theta}_\ell$ values with small adjustments $\pm\Delta_\theta$, and $\breve{\mathcal{S}}_{\varrho_\ell,\tau_\ell} \triangleq \{(\hat{\varrho}_{\ell,j} \pm \Delta_\varrho, \hat{\tau}_{\ell,j} \pm \Delta_\tau)\}_{j=1}^{\widehat{J}} \; \forall \ell = 1, 2, \ldots, \hat{L}$ comprises four pairs $(\hat{\varrho}_{\ell,j}, \hat{\tau}_{\ell,j})$ with similar adjustments $\pm\Delta_\varrho$ and $\pm\Delta_\tau$ along both in the angle and delay. By increasing the number of estimated slowly varying parameters, we effectively

35

compensate for small errors in the estimation process and encompass a broader range of potential parameters. This augmentation allows us to estimate the fast varying gains more accurately using the LS solution. We refer to this novel approach as the *subspace LS method* whose illustration is given in Figure 4.1.
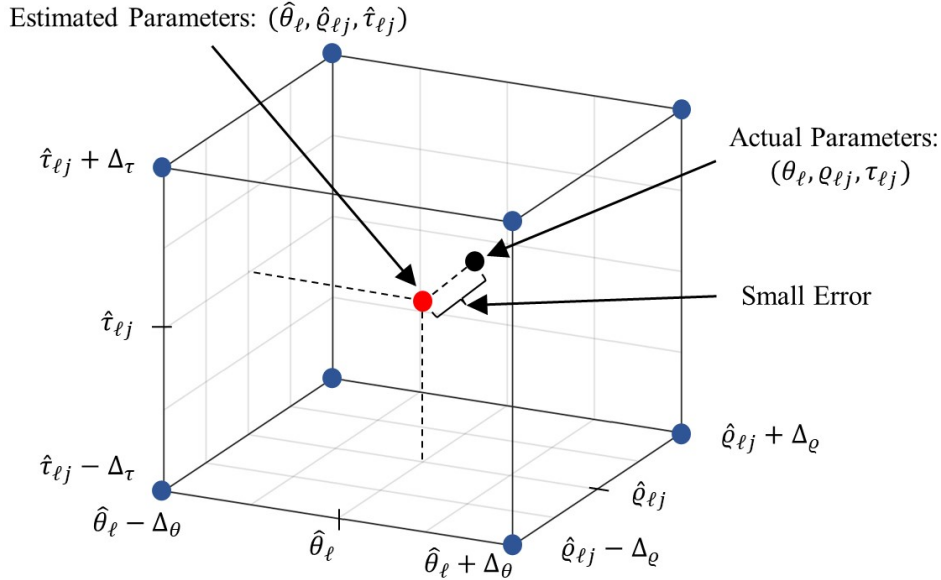

Figure 4.1: Illustration for the subspace LS method

The overview of the complete algorithm implemented within this mode, which leads to the ultimate construction of the channel, can be summarized as depicted in algorithm 3.

It is essential to highlight the point that applied methodology within this mode is expected to be relatively simple. This is because the operations conducted here are performed more frequently compared to the ST-PE mode, facilitating the capture of rapid variations. Nevertheless, considering typical values for the given system, it becomes evident that the dimensions used in the LS method are relatively high. In fact, it can be stated that the applied novel subspace LS method further increases a dimension which can be thought of as a potential drawback. The increase in dimensions contributes to a rise in the complexity imposed by this approach. However, the primary factor driving the dimensionality is the number of antennas on the BS side M, particularly in massive MIMO systems where large-scale antenna setups are utilized. Moreover, the received signal is combined directly in the digital domain without any

---

Algorithm 3 Fast Varying Channel Estimation

Input: $\mathbf{y}_{k,n} \ \forall k \in \mathcal{N}_c^{(\mathrm{f})}$ in (4.1), $\left\{\widehat{\theta}_\ell\right\}_{\ell=1}^{\widehat{L}}$ from Algorithm 1, $\left\{(\widehat{\varrho}_{\ell,j}, \widehat{\tau}_{\ell,j})\right\}_{j=1}^{\widehat{J}}$ from Algorithm 2

1: Construct $\breve{\mathcal{S}}_\theta$ and $\breve{\mathcal{S}}_{\varrho_\ell, \tau_\ell}$ (defined after (4.8))

2: Construct $\overline{\widehat{\mathbf{U}}}_k \in \mathbb{C}^{M \times 2\widehat{L}} \ \forall k \in \mathcal{N}_c^{(\mathrm{f})}$ using $\breve{\mathcal{S}}_\theta$ ($|\breve{\mathcal{S}}_\theta| = 2\widehat{L}$)

3: Construct $\widehat{\boldsymbol{\alpha}}_k \in \mathbb{C}^{8\widehat{L}\widehat{J} \times 1}$ in (4.2) using $\breve{\mathcal{S}}_{\varrho_\ell, \tau_\ell}$ ($|\breve{\mathcal{S}}_{\varrho_\ell, \tau_\ell}| = 4\widehat{J}$)

4: Construct $\widehat{\mathbf{W}}_k^{(\mathrm{f})} = \left(\overline{\widehat{\mathbf{U}}}_k \otimes \mathbf{1}_{1 \times J}\right) \mathrm{diag}(\widehat{\boldsymbol{\alpha}}_k) \in \mathbb{C}^{M \times 8\widehat{L}\widehat{J}} \ \forall k \in \mathcal{N}_c^{(\mathrm{f})}$

5: Construct $\widehat{\mathbf{W}}^{(\mathrm{f})} = [(\widehat{\mathbf{W}}_1^{(\mathrm{f})})^T, \ldots, (\widehat{\mathbf{W}}_{N_c}^{(\mathrm{f})})^T]^T \in \mathbb{C}^{M\mathcal{N}_c^{(\mathrm{f})} \times 8\widehat{L}\widehat{J}}$

6: Calculate $\widehat{\overline{\boldsymbol{\gamma}}}_n = [\widehat{\mathbf{W}}^{(\mathrm{f})}]^\dagger \mathbf{y}_n \in \mathbb{C}^{8\widehat{L}\widehat{J} \times 1}$

7: Construct $\widehat{\mathbf{W}}_k \in \mathbb{C}^{M \times 8\widehat{L}\widehat{J}} \ \forall k \in \{1, 2, \ldots, N_c\}$ following the same procedure as constructing $\widehat{\mathbf{W}}_k^{(\mathrm{f})}$ (repeat steps 2-5, including all subcarriers)

8: Construct the estimated channels: $\widehat{\mathbf{g}}_{k,n} = \widehat{\mathbf{W}}_k \widehat{\overline{\boldsymbol{\gamma}}}_n \ \forall k \in \{1, 2, \ldots, N_c\}$

Output: $\widehat{\mathbf{g}}_{k,n} \ \forall k \in \{1, 2, \ldots, N_c\}$

---

dimension reduction in this system, which indicates that the receiver beamforming structure implemented on the BS side remains fully digital. It's worth noting that this scenario can be mitigated, as demonstrated in [44], through the use of a limited number of phase shifters on the analog side. Hybrid beamforming can be employed to reduce the number of RF chains on the BS side and diminish the dimensions of the signal obtained in the digital domain, thus enhancing the greater efficiency of applied methods. However, while this aspect lies beyond the scope of this thesis, an illustrative study in the field of RIS-aided systems can be found in [45].

4.2 RIS Phase Shift Design

As previously discussed in section 3.4, it was acknowledged that a component of the channel estimation problem involves RIS phase shift design. It was further highlighted that without careful design, effective channel estimation might not be achievable. Similar to the ST-PE mode, the RIS design within the FT-PE mode has been optimized to serve the dual purpose of enhancing channel estimation accuracy and boosting data communication efficiency. Notably, in the FT-PE mode, in contrast to the ST-PE mode, the BS side possesses knowledge about the channel. Consequently,

the design emphasis shifts from scanning to directly transmitting signals between the UE and BS with optimal paths, aiming to maximize signal strength. To align with this objective, the design proposed in the study titled "A Robust Quantized Beam-Squint and Interference Aware Statistical Beamforming for RIS-Aided Massive MIMO" [reference will be given when published] has been adapted as the RIS phase shift design within the FT-PE mode. This design accounts for the phase-amplitude coupling inherent in realistic RIS structures, rendering it practically viable for our system. The suggested design optimizes the optimization metric through the implementation of the iterative phase refinement (IPR) algorithm. This approach remains sensitive to the channel's frequency selectivity and spatial wideband characteristics. Unlike the aforementioned study, our system does not encompass varying user scenarios, leading to the exclusion of interference suppression capability. Consequently, the optimization metric aims to maximize the signal-to-noise ratio (SNR) after digital processing on the receiver side, rather than the signal-to-interference and noise ratio (SINR). The applied optimization metric is formulated as follows

$$\text{SNR} = \boldsymbol{\phi}^T \left(\frac{1}{N_c} \sum_{k=0}^{N_c-1} \widetilde{\mathbf{R}}\mathbf{s}_k \right) \boldsymbol{\phi}^* \tag{4.9}$$

where $\widetilde{\mathbf{R}}\mathbf{s}_k$ is defined as the covariance matrix of the received symbol at the BS side over the kth frequency bin. In other words, the optimization algorithm that IPR runs tries to maximize the signal strength on the BS side, and a detailed explanation and formulation can be found in that study.

CHAPTER 5

PERFORMANCE EVALUATIONS

In the preceding sections, adhering to the channel estimation protocol we have adopted thus far, we completed the proposition of channel estimation methods. In essence, we initially focused on the ST-PE mode in chapter 3 to estimate the AoA and cascaded angle-delay pairs for the slowly changing parameters of the channel, and then within the FT-PE mode, we introduced the proposed methods for estimating cascaded gains in chapter 4. However, in order for these channel estimation methods to be embraced and applied, it is imperative to demonstrate their effectiveness and advantages. In this chapter, we will present the simulation results conducted for this purpose. Through these results, we will not only demonstrate the effectiveness of the proposed methods but also compare them with existing techniques. This comparison will help identify the scenarios under which our methods provide advantages. Additionally, we will provide insights into the metrics utilized for evaluating these simulation outputs and delve into the specific settings under which these simulations were conducted.

5.1 Performance Measures

To evaluate the efficacy of the proposed methods and demonstrate their distinctiveness from other techniques, the following performance metrics are employed: the cumulative distribution function (CDF) of the errors introduced in angles and delays, and the normalized mean square error (nMSE) of the reconstructed channel. The first metric, CDF, is primarily employed to assess the performance of channel estimation in the ST-PE mode. It encompasses the determination of errors in both BS-side AoA and the estimated angles and delays associated with cascaded components. By

quantifying the errors' CDF, the precision of the angle and delay estimation can be evaluated. Moreover, CDF results contribute to the detection of potential outliers. To derive the CDF results, the user's locations, i.e. all slowly and rapidly changing channel parameters, are randomly generated, and the ST-PE mode is executed on these generated channels to obtain angle and delay estimation outputs. Using these results, the weighted root mean square error (wRMSE) is computed, and then based on the calculated wRMSE values, CDF results are generated as an initial performance metric. The definition of the wRMSE can be carried out as follows

$$\text{wRMSE} \triangleq \sqrt{\sum_{i=1}^{P} \sigma_i^2 \left(\frac{1}{\sum_{k=1}^{P} \sigma_k^2} \right) |e_i|^2} \qquad (5.1)$$

where e_i represents the resulting estimation error, P stands for the total number of related MPC and σ_i denotes the average power of the associated MPC. The calculation of error is defined as $e_i \triangleq x_i - \widehat{x}_i$, where x_i is the parameter to be estimated. Moreover, the term $\sigma_i^2 \left(\frac{1}{\sum_{k=1}^{P} \sigma_k^2} \right)$ reveals that the relative power of the MPC can be considered as the weight for the ith path parameter estimation error. This is because $\sum_{k=1}^{P} \sigma_k^2$ shows the total average power of the related MPC's. Furthermore, let F denote the cumulative density function, which is defined as the probability that estimation of the parameter x yields weighted root mean square error value $wRMSE(x)$ less than or equal to s provided that parameter x is random. In a mathematical form, it can be defined as $F(s) \triangleq Pr\{wRMSE(x) \leq s\}$ for a given s. Note that $F(s)$ constitutes a proper cumulative density function as $\lim_{s \to 0} F(s) = 0$, $\lim_{s \to +\infty} F(s) = 1$, and $F(s)$ is monotonically increasing. Moreover, the critical point to emphasize here is that, instead of directly computing the CDF of the error values, a weighted RMSE definition given in (5.1) is utilized. As explained, these weights are determined based on the relative power of the given MPC. Consequently, the errors in parameter estimations for strong MPCs and those for weaker paths are not treated the same and do not contribute equally. The error in parameter estimation for a strong MPC holds more significance, thus contributing more to the RMSE calculation. This approach acknowledges the varying importance of different paths and accounts for their contributions accordingly.

The second metric nMSE is employed to determine the channel estimation perfor-

mance in the combined ST-PE and FT-PE modes. The nMSE value quantifies the accuracy of the constructed composite channel obtained by utilizing the cascaded gain estimates from the FT-PE mode along with the angle and delay parameters acquired from the ST-PE mode. These results provide a quantitative measure of the quality of the UE-to-BS effective channel estimation, achieved through successive modes involving different methodologies. This, in turn, demonstrates how accurately the user's assumed channel, which is crucial for data communication, is estimated. To compute nMSE results, the user's location remains fixed, implying that the angle and delay parameters of the channel remain constant. Consequently, the ST-PE mode is executed once, and the stationary parameters are estimated. Subsequently, channel gains are randomly generated, and for each generated value, estimations are made within the FT-PE mode. These estimations are then averaged to obtain the nMSE results. Further, user locations are also randomly generated to compute *average nMSE* values. The metric referred to as nMSE in the upcoming sections pertains to these obtained average nMSE values. For a given user location, the nMSE can be defined as

$$\text{nMSE} \triangleq \frac{\mathbb{E}_{\mathbf{n},\gamma}\left\{\|\mathbf{g} - \hat{\mathbf{g}}\|^2\right\}}{\mathbb{E}_{\mathbf{n},\gamma}\left\{\|\mathbf{g}\|^2\right\}} \tag{5.2}$$

where $\mathbf{g} \in \mathbb{C}^{MN_c \times 1}$ matrix can be obtained by combining the composite channels $\mathbf{g}_k$ over all subcarriers utilized as $\mathbf{g} \triangleq \begin{bmatrix} \mathbf{g}_1^T & \mathbf{g}_2^T & \ldots & \mathbf{g}_{N_c}^T \end{bmatrix}$. Additionally, the given nMSE calculation can be analytically computed and expressed in a closed form as follows

$$\text{nMSE} = \frac{\text{Tr}\left\{\mathbf{W}^H\mathbf{P}_{\hat{\mathbf{W}}}^{\perp}\mathbf{W}\mathbf{R}_\gamma\right\} + N_0 LJ}{\text{Tr}\left\{\mathbf{W}^H\mathbf{W}\mathbf{R}_\gamma\right\}}, \tag{5.3}$$

Proof. See Appendix B. □

where $\mathbf{R}_\gamma \triangleq \mathbb{E}_\gamma\left\{\gamma\gamma^H\right\}$ is the covariance matrix of the fast-varying channel gains. Note that when the channel gains are uncorrelated then $\mathbf{R}_\gamma$ becomes a diagonal matrix.

5.2 Numerical Settings

In order to obtain simulation results, specific scenarios have been created under which proposed methodologies are evaluated. These scenarios are shaped by the values of the parameters present in the system model. To ensure the reproducibility of results and facilitate ablation studies, having knowledge of these parameter values is of paramount importance. Therefore, this section provides the numerical values attributed to these parameters. As described in chapter 2, both the BS and RIS possess ULA-type antennas with a total of $M = N = 100$ elements each. In contrast, the user is equipped with a single antenna. The antenna element spacing is set to $\lambda/2$ for both the RIS and BS sides. Notably, the communication link connecting the BS and RIS consists of two MPCs, each characterized by relative average power levels set at $0\ dB$ and $-3\ dB$, respectively. On the other hand, the communication channel between the RIS and UE is formed by three MPCs, with their relative average power levels specifically set at $0\ dB$, $-3\ dB$, and $-5\ dB$. The Rician factor K is set to 10 dB for each MPC between the BS and RIS, as well as between the RIS and UE. The channel angle parameters are uniformly sampled from the range of $[-60, 60]$ degrees. Similarly, the channel cascaded delay parameters are uniformly distributed between 0 and 24. The practical RIS phase shift parameters in equation (2.9) are tuned as in the study of [36]. Specifically, $\beta_{\min}$ is assigned a value of 0.2, ϕ_0 is set at 0.43π, and α_0 is chosen as 1.6. Within the FT-PE mode, the IPR algorithm used for RIS phase shift design operates over 40 iterations, ensuring the convergence of the design process. In the context of the ST-PE mode, the number of beams T is aligned with the number of antennas on the RIS, being set at 100. The OFDM symbol block length is set to 480, while within the both ST-PE and FT-PE modes, only 48 subcarriers are allocated for channel estimation. The efficient implementation of the OMP algorithm in the ST-PE mode has also user-defined parameters. These include an angle grid size of 200 and a delay grid size of 50, with the algorithm refining its dictionary through 4 iterations. In the subspace LS method, precise compensation amounts are selected, employing ± 0.01 degrees for angle estimation and ± 0.01 sec/Hz for delay estimation. Also, unless explicitly specified, the default values of 10 for f_c/W and $20\ dB$ for the SNR are applied, establishing a consistent benchmark for comprehensive evaluation and comparison. Finally, We characterize the SNR as the ratio between the average sig-

Table 5.1: Default values of the simulation parameters

PARAMETERS	VALUE
# of antenna at BS (M)	100
# of antenna at RIS (N)	100
Antenna Spacing	$\lambda/2$
# of BS-RIS MPC (L)	2
# of RIS-User MPC (J)	3
Relative Power Levels of BS-RIS MPCs	0 dB | -3 dB
Relative Power Levels of RIS-User MPCs	0 dB | -3 dB | -5 dB
Rician Factors (K)	10 dB
Channel Angle Parameters Range	[-60, 60] degrees
Channel Delay Parameters Range	[0, 12]
OFDM Block Length	480
# subcarriers in ST-PE Mode	48
# subcarries in FT-PE Mode	48
# of beams in ST-PE Mode	100
SNR	20 dB
fc/W	10

nal power obtained by the user through each RIS element and the noise power. The formulation can be expressed as follows

$$\text{SNR} \triangleq M E_s \left(\sum_{\ell=0}^{L} \left(\overline{\mu}_\ell^2 + \overline{\alpha}_\ell^2 \right) \right) \left(\sum_{j=0}^{J} \left(\mu_j^2 + \alpha_j^2 \right) \right) \frac{1}{N_0} \qquad (5.4)$$

where E_s stands for the average symbol power of the user which is taken as unit power. Moreover, the term M in this formula represents the contribution of beamforming applied at the BS. This emphasizes that the SNR is defined for the user after the application of BS beamforming. Additionally, it's worth mentioning that the amplitudes of RIS elements are considered as unity in the SNR definition. This simplification is made solely for the purpose of defining SNR. The parameters setting is summarized in table 5.1.

5.3 Simulation Results

In order to enhance the meaningfulness of our simulation results and establish a frame of reference for our proposed methodologies, it becomes useful to demonstrate the other state-of-the-art solutions. This demonstration aims to show the advantages and disadvantages of the methods we propose under different conditions. To achieve this, we adapted and integrated the methods from a relevant contemporary work [24] into our simulations. From that study, we specifically focused on angle estimation methods, particularly the technique employed for AoA estimation and the OMP method used for cascaded angle estimation. We denoted the AoA estimation method as the conventional AoA estimation technique (Conv. AoA Est.), and the OMP method as the conventional OMP method (Conv. OMP) within our study. Both the Conv. AoA Est. and Conv. OMP methods were adjusted to function effectively with OFDM, thus enhancing their capability to handle frequency-selective channels. However, it's important to note that these two methods exhibit unawareness against the beam-squint effect. In other words, they attempt to estimate the same angle for every subcarrier without considering the frequency-dependent nature of angles. In addition, the OMP technique was also executed using the efficient implementation proposed in section 3.2, aiming to save computational time. On the other hand, the Conv. OMP in the training mode assumes fully correlated MPC gains across all consecutive time instances, which renders it unaware of potential decorrelation. In contrast, the Conv. The AoA Est. technique does not encounter such unawareness, as the effective channel inherently changes at each time instance, a factor already addressed in AoA estimation. We will compare the results of the adapted AoA method with the proposed AoA estimation method, namely the beam-squint aware AoA estimation (BSA AoA Est.), which takes into account the beam-squint effect. Additionally, we will compare Conv. OMP results in our study consider both the beam squint effect and the decorrelation that can arise during the training mode. For this latter study, we have named it the beam-squint aware modified-OMP (BSA-MOMP) method. For these methods that can perform slow time parameter estimation, their specification is summarized in table 5.2. In the context of FT-PE mode, we took conventional least squares (Conv. LS) solutions as well as a genie-aided conventional LS (Genie-aided LS) approach, where channel parameters were assumed to be perfectly known, as reference bench-

44

Table 5.2: Specification of the methods that can perform ST-PE

ST-PE METHODS	BEAM-SQUINT AWARENESS	DECORRELATION AWARENESS
Conv. AoA Est.	✗	N/A
BSA AoA Est.	✓	N/A
Conv. OMP	✗	✗
BSA-MOMP	✓	✓

Table 5.3: Summary of the methods that can perform FT-PE

FT-PE METHODS	DESCRIPTION
Conv. LS	direct slowly changing parameter estimation
SA – LS	augmented slowly changing parameter estimations
Genie-Aided LS	perfect slowly changing parameters

marks. By incorporating these solutions in our simulations, we were able to compare them against our proposed subspace-aware LS (SA-LS) method. Additionally, we combined these methods with slow-time estimation techniques, which resulted in distinct methodological variations. For instance, when considering slow-time parameter estimation while being aware of the beam-squint effect as proposed, and channel construction involved using conventional LS, then it was named the beam-squint aware modified OMP-aided LS method (BSA-MOMP aided Conv. LS). Similar naming conventions were applied for scenarios without beam-squint consideration, such as beam-squint unaware Conv. LS (Conv. OMP aided Conv. LS). That means they utilize the methods in ST-PE mode as proposed in [24]. Similarly, our proposed subspace LS method was addressed differently depending on the slow-time estimation method used as well. For beam-squint aware cases, it was denoted as beam-squint aware modified OMP-aided subspace aware LS (BSA-MOMP aided SA-LS), while for scenarios without beam-squint consideration, it was termed beam-squint unaware OMP-aided subspace aware LS (Conv. OMP aided SA-LS). In table 5.3, the summary of these methods is given.

That means they utilize the methods in ST-PE mode as proposed in [24]. Similarly, our proposed subspace LS method was addressed differently depending on the slow-

45

time estimation method used as well. For beam-squint aware cases, it was denoted as beam-squint aware modified OMP-aided subspace aware LS (BSA-MOMP aided SA-LS), while for scenarios without beam-squint consideration, it was termed beam-squint unaware OMP-aided subspace aware LS (Conv. OMP aided SA-LS). Next, we present our results obtained through extensive simulations.

Firstly, we direct our attention towards the evaluation of channel angle estimation errors within the context of the ST-PE mode. Figure 5.1 presents the results for the following scenario: MPC channel gains are not decorrelated over time across different OFDM symbols and remain fully correlated in the extreme scenario. The SNR is set at $20\ dB$, while the parameter fc/W, rather than being held constant, is manipulated to be 10 to simulate the beam squint effect, and 1000 to denote scenarios where this effect is practically negligible, as previously delineated. To derive this figure, the CDF of weighted RMSE values for angle estimation errors has been computed. Parts a and b of this figure include the results of different RIS configurations; in part a, RIS is considered ideal, while in part b, RIS is discussed with practical concerns. It is evident from these results that, under the influence of beam squint i.e. $fc/W = 10$ conventional angle estimation methods, namely Conv. AoA Est. and Conv. OMP, exhibits poor performance, as indicated by the solid lines in the figure. This poor performance is consistent across both ideal and practical RIS structures, demonstrating that conventional methods struggle in systems affected by beam squint, regardless of the RIS type. In the absence of beam squint, that is, in narrowband systems simulated by taking the fc/W value as 1000, the results of conventional angle estimation methods and the proposed methods overlapped. This situation can be seen with the dashed lines on the figure and it confirms our simulation setup because conventional methods perform well as expected in the absence of beam squint, meaning that there is no open point in the implementation of these methods. However, it is essential to point out that the proposed methods exhibit relatively better performance in scenarios where there is even a minor presence of the beam squint effect compared to scenarios entirely free of the beam squint effect. This phenomenon can be attributed to the diversity introduced by the beam squint effect, as it allows for the acquisition of different channel-related information from different subcarriers. Another notable point is that the results obtained with an ideal RIS configuration are slightly more

sensitive than those obtained with practical RIS configurations. This difference arises from the presence of phase-amplitude coupling, which is inherent in practical RIS designs and is not considered in the SNR definitions governing the simplicity principle. As previously mentioned, phase-dependent losses occurring on the RIS surface lead to a reduction in the effective SNR at the receiver, consequently affecting angle estimation precision. In addition to these aspects, another point to consider is that AoA estimation outperforms cascaded angle estimation. Several factors contribute to this observation. Firstly, the resulting AoA and the number of cascaded angles may be different. Moreover, while AoA estimation methods only estimate AoA, cascaded angles are estimated through the OMP method together with cascaded delay parameters. In other words, the number of parameters estimated by the methods applied for both components is different, which may be a reason for the difference in their performances. Secondly, AoA estimation is performed initially and can utilize observations from all antennas at the system's inception. In contrast, for OMP operation, projection is conducted after AoA estimation, necessitating the amalgamation of data received from antennas at different time instances. Consequently, while AoA estimation can utilize data from various antennas within a single time instance, OMP aggregates information from different time instances, introducing another dimension of variability within the observation space, which contributes to performance differences.

In figure 5.2, similar to figure 5.1, the CDF results of angle estimation errors obtained from the applied angle estimation methods within the ST-PE mode are presented. The overall scenario remains the same, with the only difference being the observed decorrelation in MPC gains. This time, MPC gains are considered fully decorrelated as they change at each time instance, located on the other side of the extreme scenario. In this figure, as in the previous results presented in Figure 5.1, conventional methods do not perform well under the beam squint effect. Up to this point, no significant differences are expected compared to the previous results. However, even in the absence of beam squint, the Conv. The OMP method does not yield satisfactory results. The reason for this is the decorrelation occurring in MPC gains. The conventional OMP method processes observations obtained at different times coherently, meaning it is not aware of the potential decorrelation. Since the observations change over time, when processed coherently, they can have a destructive effect on each other. This un-
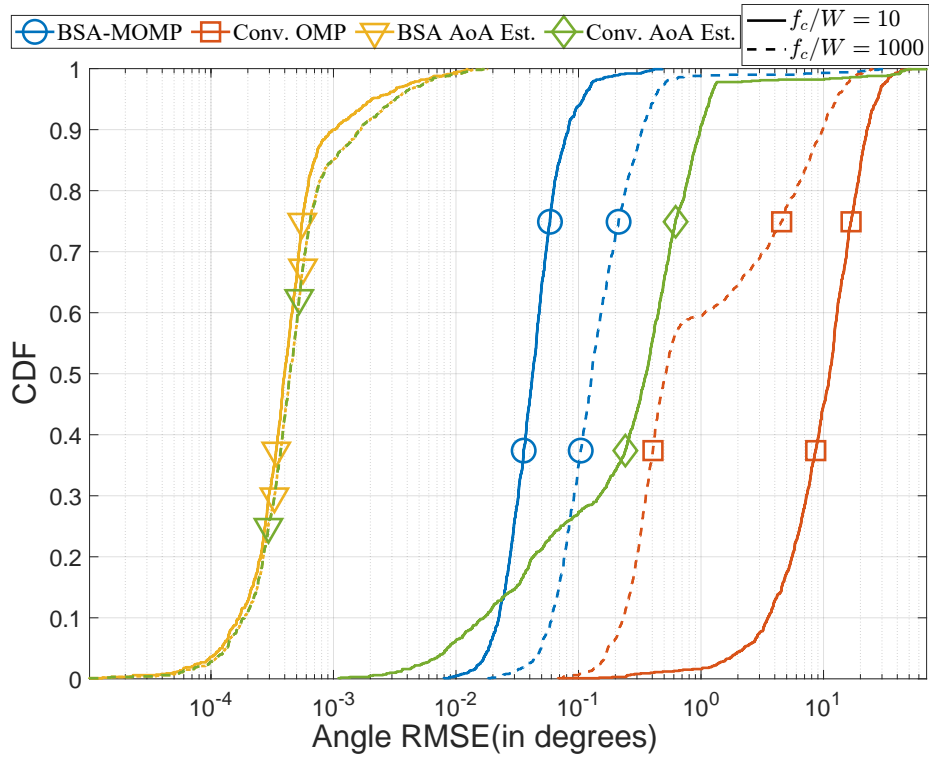
47
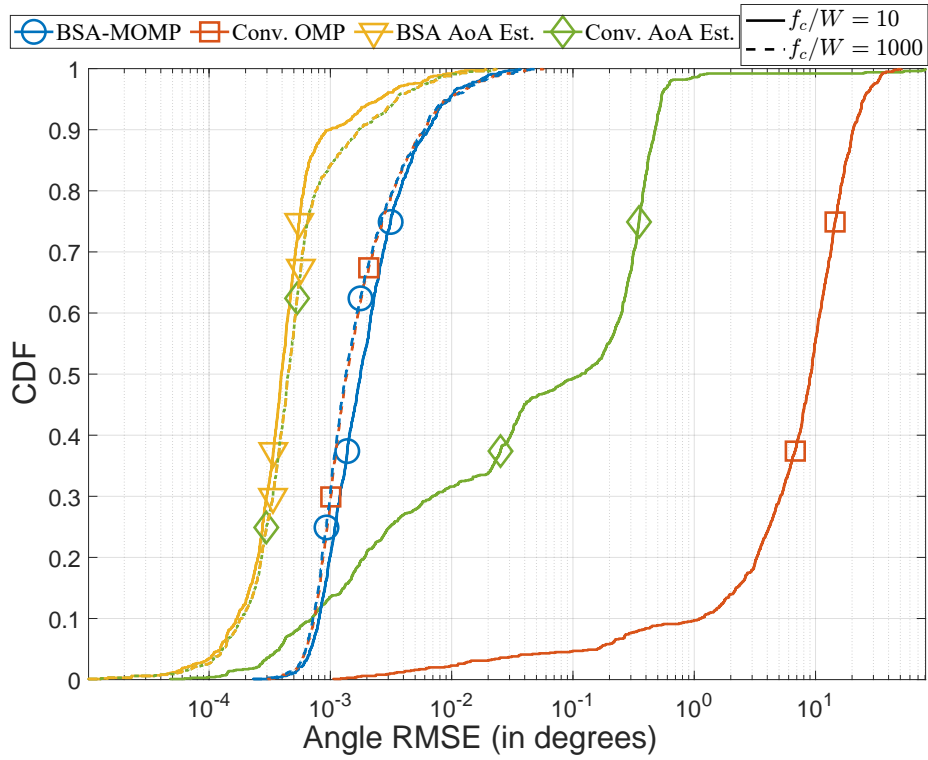
(a) with ideal RIS structure
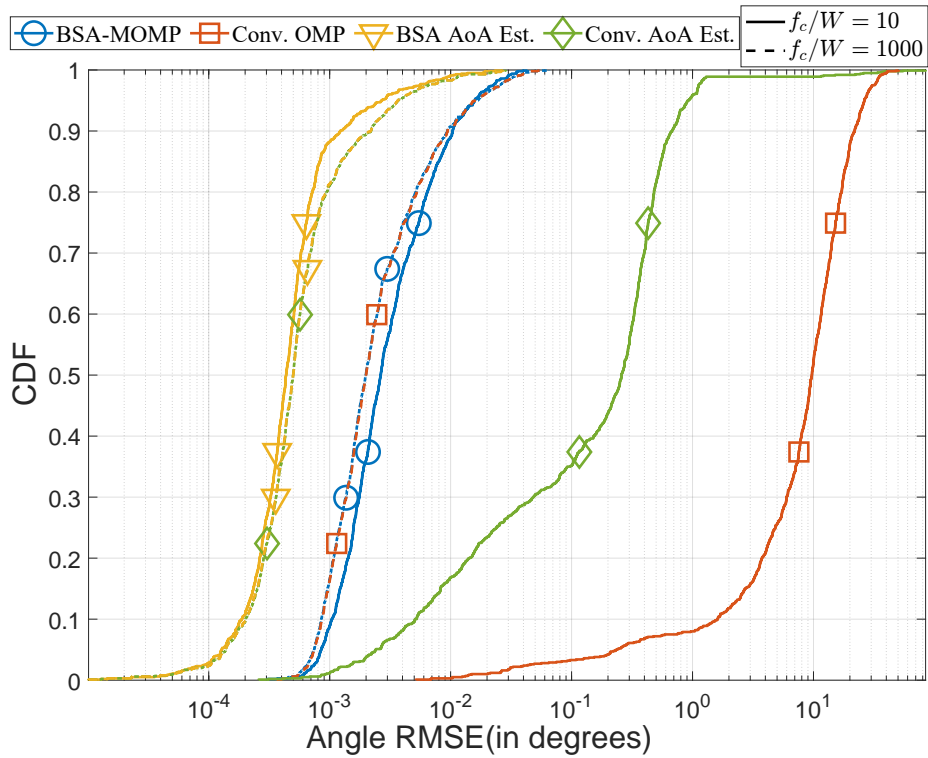
(b) with realistic RIS structure

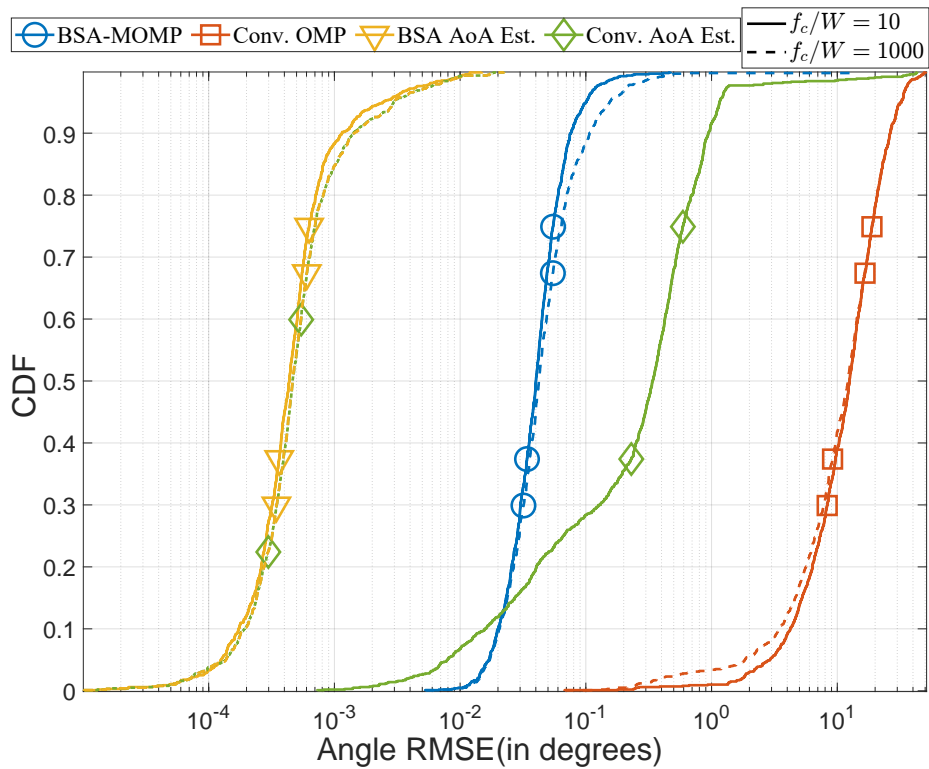Figure 5.1: CDF of the angle estimation error when MPC gains are fully-correlated with $SNR = 20\,dB$.

derscores the importance of considering decorrelation as a factor that should be taken into account; otherwise, a severe performance loss can be encountered.

Motivated by this situation, the proposed BSA-MOMP method addresses this issue by processing decorrelated observations in a non-coherent manner, mitigating the performance loss to some extent, even though there is still a slight performance loss compared to the correlated case. However, this slight performance loss is a result of the observations we have at hand, indicating that it is a trade-off arising from the decorrelated condition. On the other hand, there is no such distinction for AoA estimation. By its nature, AoA estimation methods encounter different effective channel gains at different times. For instance, the use of a different RIS configuration at each time instance alone is sufficient to demonstrate this. Therefore, these methods generally do not directly combine observations obtained at different times but rather process them non-coherently. It is not possible to speak of a severe performance loss in AoA estimation performances in this extreme scenario, as can be readily observed from the provided figure.

Another set of results obtained after the CDF analysis involves the nMSE versus fc/W results. Firstly, in figure 5.3, nMSE results are presented for different fc/W values when channel reconstruction is performed along with the operation of ST-PE and FT-PE modes. Similar to the CDF results, in this scenario, MPC gains are fully correlated. The SNR is set to its default value of $20\ dB$. Parts a and b also present results obtained from different RIS configurations. From the results, it is evident that the genie-aided LS method outperforms all other methods. This outcome is expected since, within this method, we have perfect knowledge of channel components, and it is not expected that any other method can provide better estimation under these circumstances. On the other hand, as shown in dashed lines along with the results of conventional methods, methods performing angle estimation exhibit poor performance when Fc/W is low, but their performance improves as this value increases. As previously mentioned, beam squint is a phenomenon encountered in wideband systems and higher fc/W values correspond to narrowband scenarios. Therefore, angle estimation methods that do not consider the beam squint effect have demonstrated good performance in narrowband systems, resulting in this performance trend. This effect has been observed independently of the RIS configuration, as expected, in both
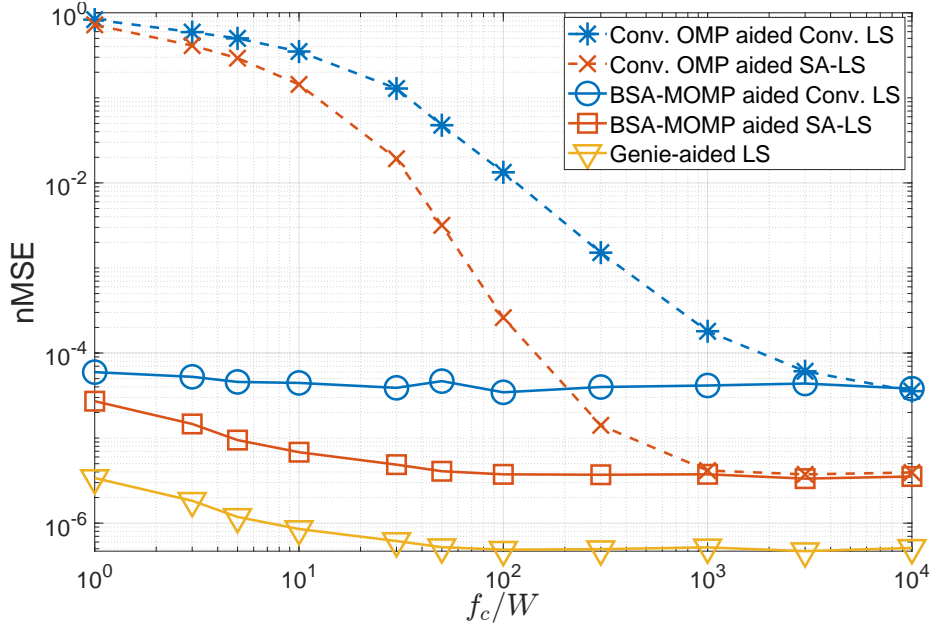
(a) with ideal RIS structure
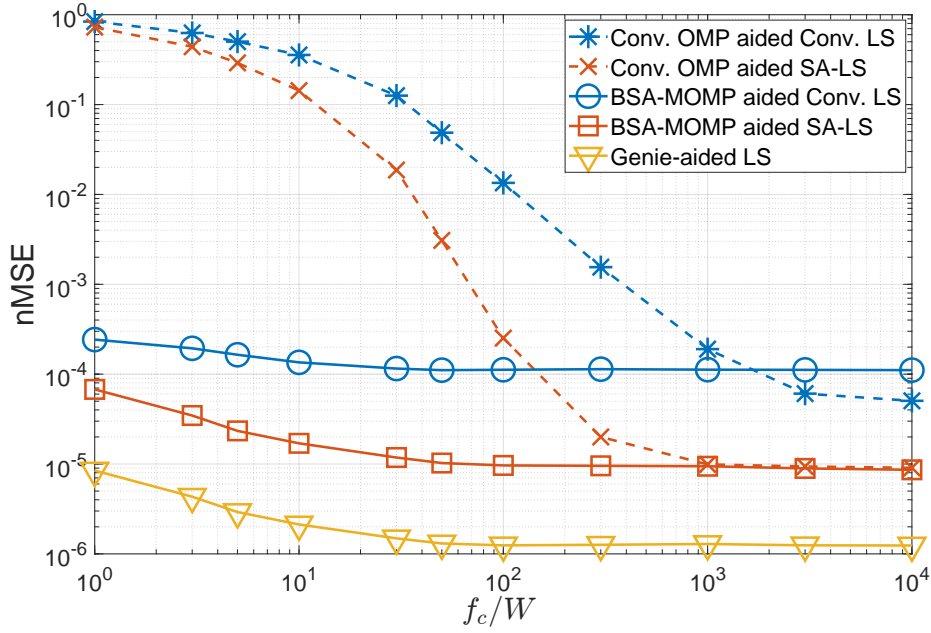

(b) with realistic RIS structure

Figure 5.2: CDF of the angle estimation error when MPC gains are fully-uncorrelated with $SNR = 20\ dB$.

parts. However, methods that complete channel reconstruction by performing angle estimation along with the proposed methods, shown with solid lines, do not show significant changes based on the fc/W value. This is because they consider the beam squint effect and do not anticipate severe performance degradation. Among these methods, the proposed SA-LS method outperforms the naive LS method. In other words, the proposed method compensates for the angle and delay estimation errors that affect the LS method by increasing the dimensions of the estimation space. This demonstrates the effectiveness of the proposed method and how it boosts the LS method, approaching LS performance to the genie-aided method result. The final point to be emphasized from this figure is the convergence of dashed and solid lines. It is noticeable that, except for the practical RIS-based conv. LS method, as fc/W increases, the results of methods using the proposed and conventional methods as a basis tend to converge, as expected. However, in the exceptional case mentioned, the conventional LS method for angle estimation outperforms the LS method for angle estimation with the proposed method at higher fc/W values. This situation requires further investigation, particularly regarding data acquisition, and should be addressed as part of future work.

Another set of results, depicting nMSE values according to the fc/W ratios, is presented in figure 5.4. Similarly, this figure illustrates the nMSE values resulting from the channel reconstruction after running the ST-PE and FT-PE modes. The scenario remains largely similar to figure5.3, with the exception that in this extreme scenario, MPC channel gains are considered fully decorrelated. That means at each time instance the gains of the MPCs are changing. Upon examining the results, it is evident that, as expected, the genie-aided method performs well among all methods. The proposed methods exhibit consistent performance across varying Fc/W values in a similar manner. On the other hand, as previously observed in the CDF plots, conventional methods perform poorly even if the beam squint effect is absent. The results presented in this figure parallel those from the CDF plots. This correlation stems from the fact that, as seen in figure 5.2, when MPC gains become decorrelated, conventional methods, which perform cascaded angle estimation, fail. This effect propagates into the FT-PE mode, leading to reduced channel estimation quality and higher nMSE values. It's worth noting that even the novel SA-LS method, proposed for angle estimation,
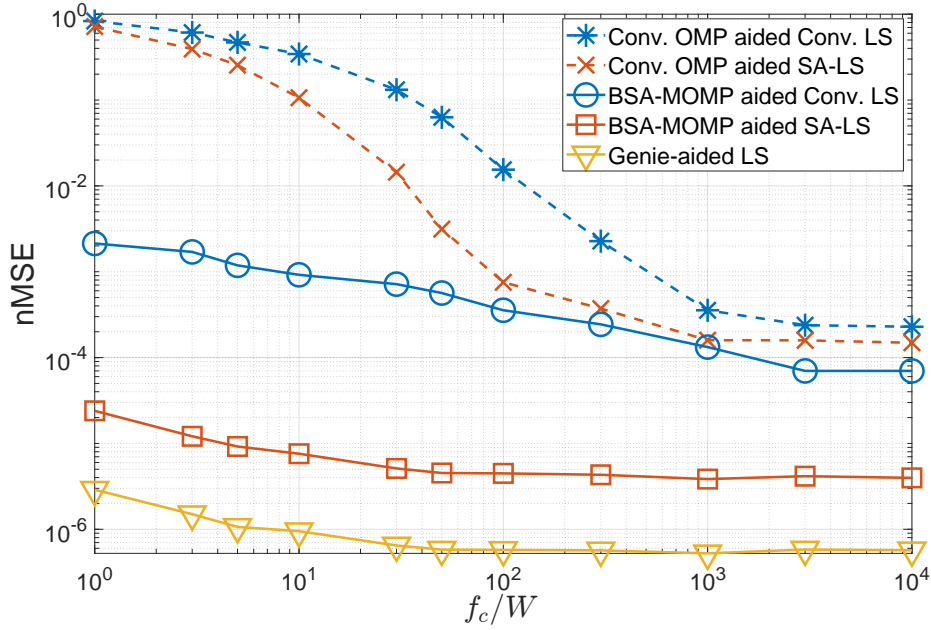
(a) with ideal RIS structure
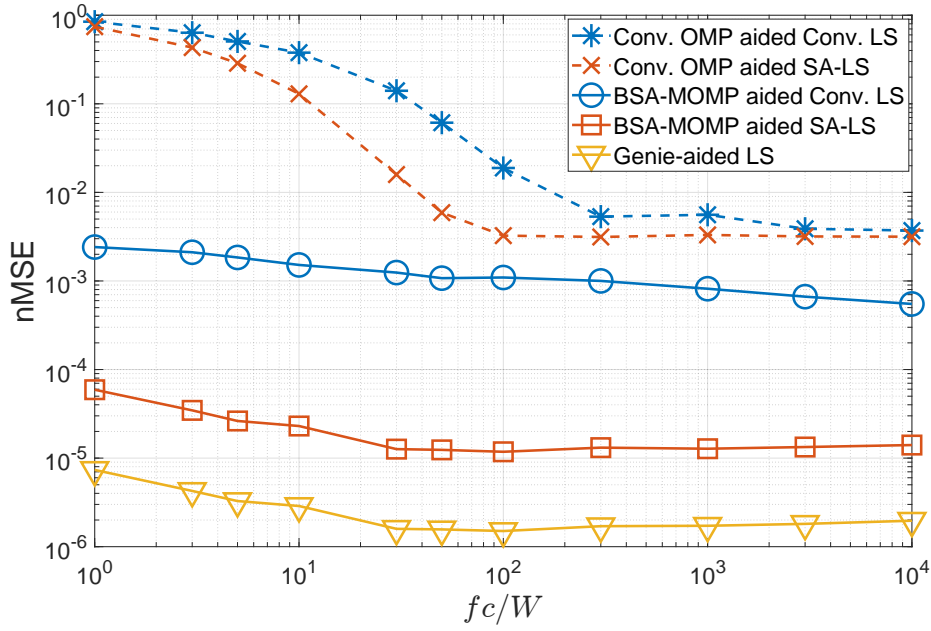

(b) with realistic RIS structure

Figure 5.3: nMSE versus reciprocal of the fractional bandwidth when MPC gains are fully-correlated with $SNR = 20\,dB$.

doesn't provide a solution in this case. The errors in angle estimation adversely affect the RIS design within the FT-PE mode, rendering them uncompensatable. However, when angle estimation is performed using the BSA-MOMP method, which considers decorrelation through non-coherent techniques, the decrease in angle estimation accuracy observed in the CDF plots coincides with the higher nMSE values in the conv. LS method. The proposed SA-LS method also manages to mitigate this decrease to some extent, as it compensates for angle estimation errors. This reiterates the effectiveness of the proposed method and its robustness against extreme scenarios. Lastly, it's worth noting that these observations remain consistent in parts a and b, highlighting that the results are independent of the specific RIS design.

In the following results, nMSE values are presented once again, but this time with a variation in the SNR values, rather than the fc/W ratio. This provides an opportunity to compare the performance of the proposed and conventional methods under different SNR conditions. In figure 5.5, nMSE values obtained after running the ST-PE and FT-PE modes are plotted for various SNR values. The fc/W value is held constant at 10 to simulate the beam squint effect, while MPC channel gains remain fully correlated in this extreme scenario, following the OFDM symbol times. As observed from the results, the genie-aided method performs the best across all SNR values, as explained earlier due to the perfect knowledge of channel components. When we follow the dashed lines, it's evident that conventional methods and methods performing angle estimation saturate at high nMSE values. This is because they ignore the beam squint effect, irrespective of SNR. Even if we operate at a very high SNR value, it's impossible to achieve a good nMSE result with these methods when this effect is not considered. This highlights the importance of accounting for the beam squint effect. Increasing SNR incurs a certain cost, and investing in it without considering the right factors doesn't yield the desired results. Similar results can be observed in parts a and b since this phenomenon occurs independently of the RIS structure. The performance of methods performing cascaded angle estimation, based on the BSA-MOMP method, shows a certain trend depending on SNR. Especially in the low SNR range, the proposed SA-LS method doesn't provide any additional performance gain over the conv. LS method; in fact, it performs even worse. This can be explained as follows: the SA-LS method, as mentioned earlier, increases the dimension of the estimation
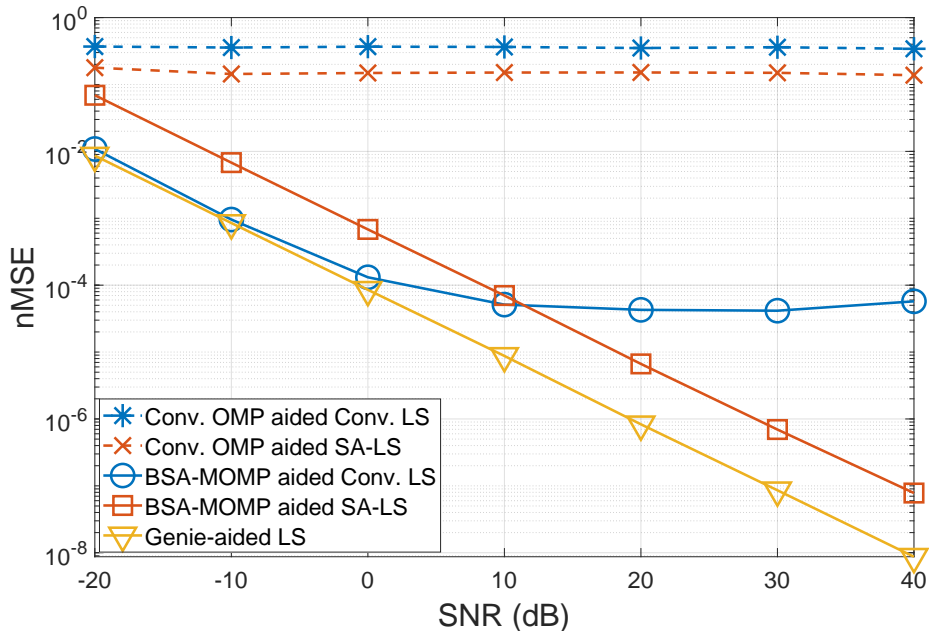
(a) with ideal RIS structure

(b) with realistic RIS structure

Figure 5.4: nMSE versus reciprocal of the fractional bandwidth when MPC gains are fully-uncorrelated with $SNR = 20\ dB$.

space. Consequently, the effective noise space also increases. In the low SNR regime, the received signal power is insufficient, and the SA-LS method results in a poorer performance. However, in the high SNR regime, the performance achieved with the conv. LS method saturates. In other words, the LS method has a performance limit, that it cannot surpass due to angle estimation errors. But with the proposed SA-LS method, this limit is exceeded, and as SNR increases, performance improves, closely approaching the genie-aided method. From these points, it can be readily concluded that if we are running our system with SNR above a certain threshold, the SA-LS method can provide results close to the genie-aided performance.

The results obtained in figure 5.5 have been replicated in a scenario where fully correlated MPC gains are now taken as completely uncorrelated and varying at every time instance as in the CDF results and nMSE vs. fc/W results. These replicated results are presented in figure 5.6. As observed from the results conventional methods yield high nMSE values, indicating a significant performance loss. This poor performance is attributed to their failure to account for both the beam squint effect and the decorrelation among MPC gains. On the other hand, the genie-aided method remains unaffected by the consideration or lack thereof of decorrelation during angle estimation in the OMP method, continuing to be the best-performing method. This is because it operates again with the assumption that angle and delay components are perfectly known as mentioned previously. However, in the case of methods employing OMP while considering both the beam squint effect and the mentioned decorrelation, differences are noticeable. The BSA-MOMP-based conv. LS method encounters a slight performance loss, as mentioned previously in terms of CDF performance. Nevertheless, the SA-LS method mitigates this situation, especially in the high SNR region, preventing the performance loss observed in conv. LS concerning SNR and approaching the performance of the genie-aided method. These results also demonstrate once more that this novel proposed method operates robustly concerning decorrelation.

In all the results given so far, the RIS structure in both CDF, nMSE vs fc/W, and nMSE vs SNR plots have been studied separately, taking into account ideal and practical concerns. Their results obtained are also presented separately. Figure 5.7 has been added to answer the question of what if the phase-amplitude coupling effect,
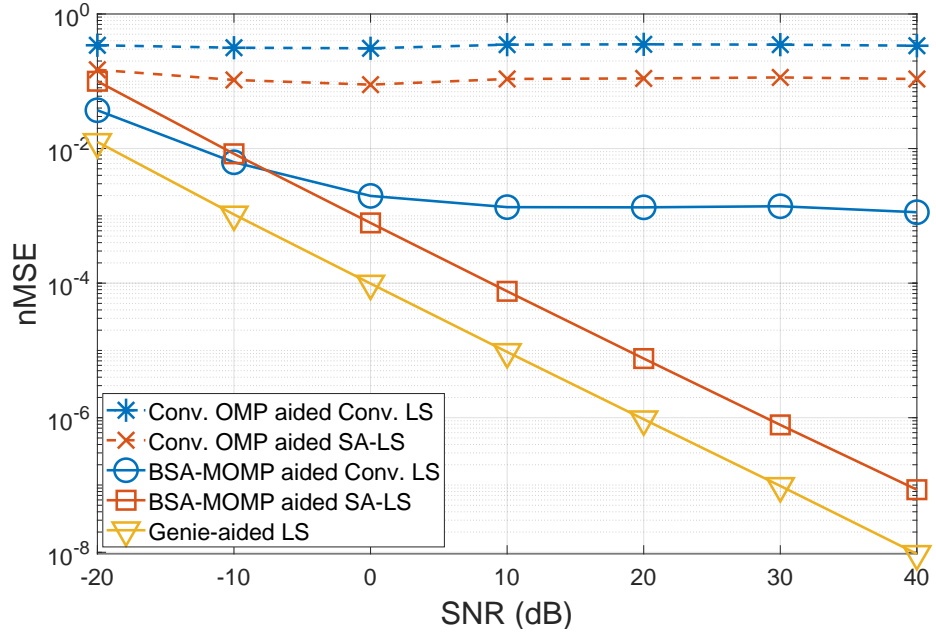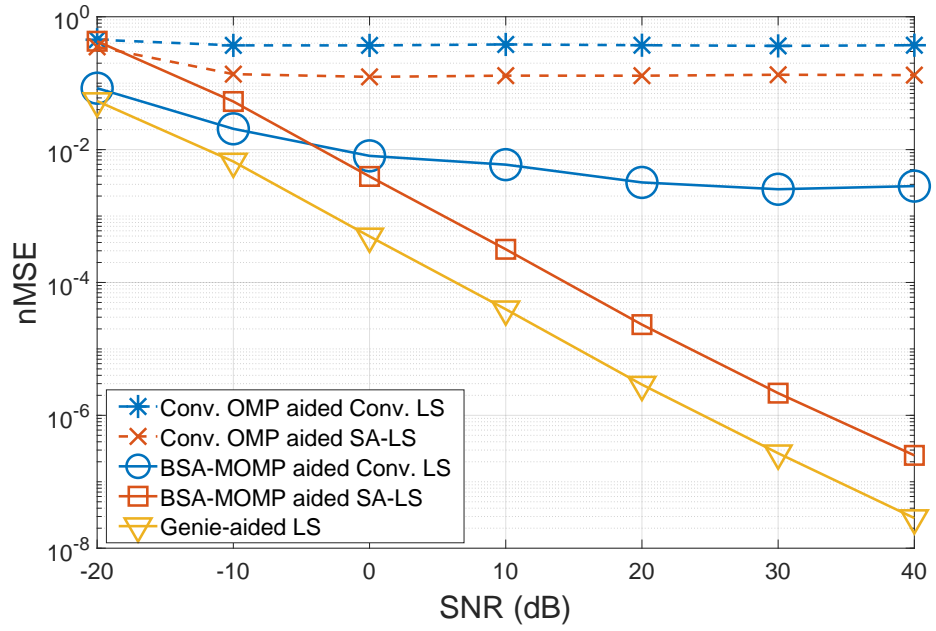
(a) with ideal RIS structure
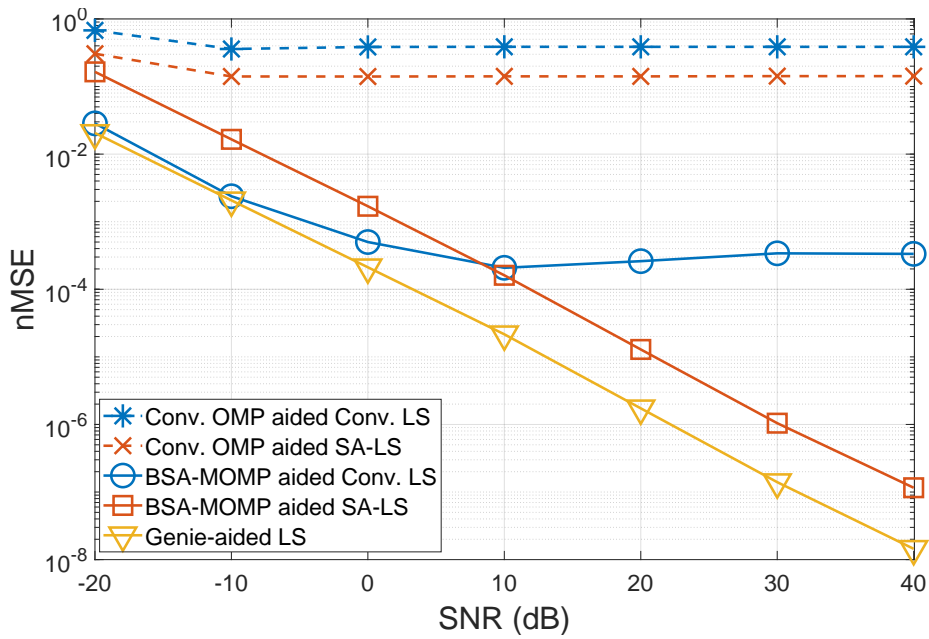
(b) with realistic RIS structure

Figure 5.5: nMSE versus signal-to-noise ratio when MPC gains are fully-correlated with $fc/W = 10$.

(a) with ideal RIS structure

(b) with realistic RIS structure

Figure 5.6: nMSE versus signal-to-noise ratio when MPC gains are fully-uncorrelated with $fc/W = 10$.

which exists in RIS hardware designs in practice, is ignored and channel estimation is done in this way. In these results, SNR values were varied, and the fc/W value was set to 10 to indicate the presence of the beam squint effect. Results for both extreme scenarios of MPC gains were presented, with dashed lines representing the case where MPC gains are completely decorrelated and solid lines representing the case where these gains are completely correlated. The RIS design within the channel is considered ideal by the user, and while the design is made with this assumption, the RIS operates with the amplitude-phase coupling that actually exists on it. This difference is encountered in both ST-PE and FT-PE modes. Looking at the results, it can be seen that a different name, channel estimation with perfect ST-PE, is used for the genie-aided method. The reason for this is that this method is no longer aware of the difference in the RIS design but still perfectly estimates the channel parameters estimated within the ST-PE mode. Hence, this nomenclature has been adopted. While this method appeared as the best-performing method in the other provided figures, making such an interpretation is not possible in the context of these results. This situation demonstrates how crucial it is to consider the practical amplitude-phase effect existing in RIS. For the other methods, it is difficult to discern a specific trend. Despite considering beam squint and decorrelation, these methods, as SNR increases, experience some improvement in performance, but they saturate at high nMSE values. In other words, increasing SNR does not become a solution. In summary, just like effects such as beam-squint and MPC gain variations, addressing this amplitude-phase coupling condition encountered in practical RIS elements is highly significant.

One of the RIS deployment scenarios that come to mind is placing the RIS closer to the BS, allowing the RIS to directly receive signals from the BS, especially serving users with blocking objects between them and the BS through the RIS. In such a scenario, the amount of scattering between the BS and the RIS will be limited, leading to a predominantly LOS channel [46]. We conducted simulations under such conditions and shared the results in figure 5.8. Due to the dominance of LOS, the LOS channel was simulated to work almost losslessly by creating a single MPC between the BS and the RIS with the gain of unity. Results were generated by changing SNR values, and in these results, the fc/W value was set to 10 again to create a scenario under the influence of the beam-squint effect. Particularly, the MPC gains between
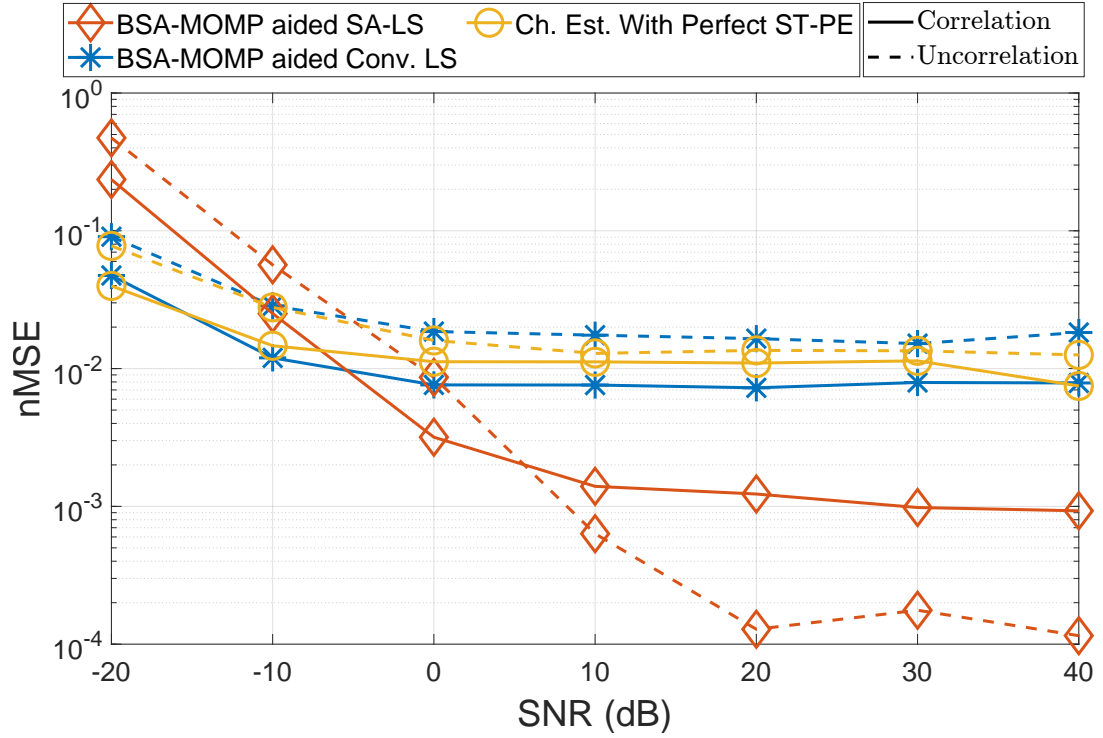
58

Figure 5.7: nMSE versus signal-to-noise ratio when realistic RIS properties are ignored with $fc/W = 10$.

the RIS and the User were fully correlated to create an easier scenario. Based on the results, it seems that the outcomes are as expected. Similar to previous results, the results shown with dashed lines saturate at high nMSE values due to ignorance of the beam-squint effect. Based on the results shown with solid lines, the conventional LS method performs well in the low SNR region but reaches its performance limit as SNR increases. In this SNR region, the proposed SA-LS method enhances the performance of the LS method, achieving results close to the genie-aided method. The genie-aided method delivers the best results with perfect channel knowledge. The parallelism in the results indicates that even in scenarios where the RIS is positioned near the BS, our system operates as expected. Furthermore, considering the other results, the fact that there is no noticeable change in the results with an increase in the number of paths and scattering between the BS and the RIS suggests that this situation is not a bottleneck.

As mentioned earlier, the emergence of the beam squint effect generally requires two conditions to be met: the system operating bandwidth should be wide, and there
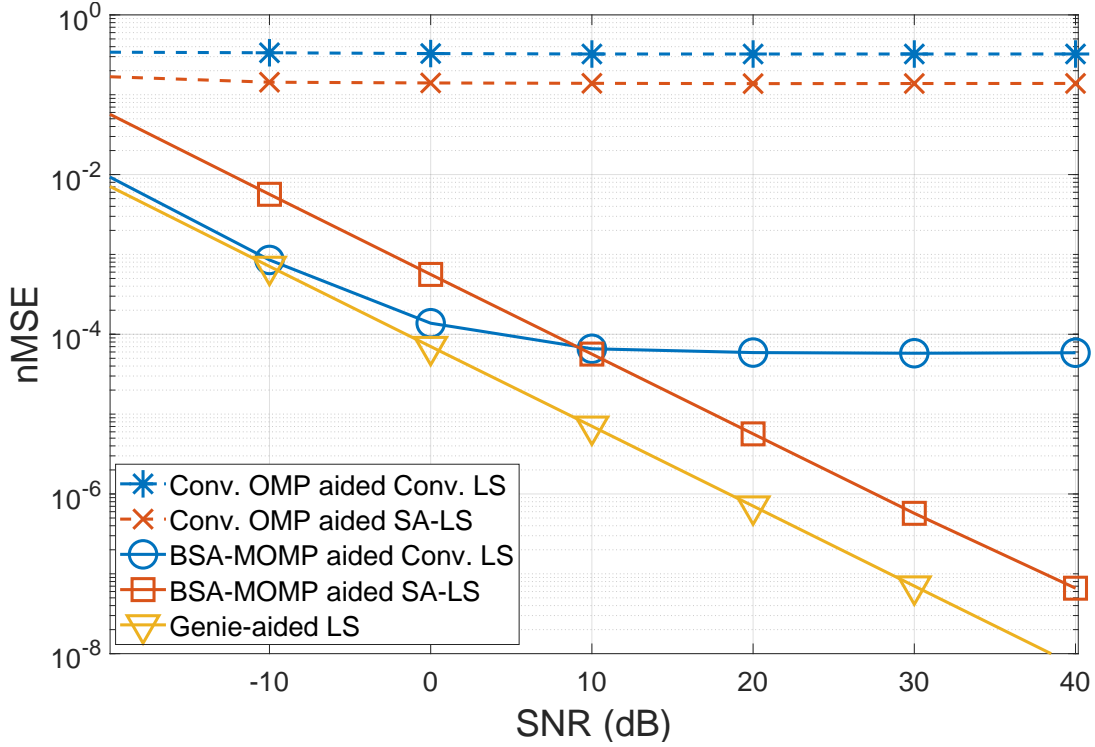
Figure 5.8: nMSE versus signal-to-noise ratio under BS-RIS LOS dominance with $fc/W = 10$.

should be a large number of antennas in the array structure. In previous results, the bandwidth of the system was expanded or narrowed to either increase or decrease the beam squint effect, while keeping the number of antennas constant. By changing the number of antennas, the beam-squint effect can also be mitigated or intensified. In figure 5.9, results obtained by manipulating the beam squint effect in this manner are presented. Similarly, SNR and fc/W values were set to their default values, which are $20\ dB$ and 10, respectively. The MPC gains were taken to be correlated over time to ensure that conventional methods are not affected by this condition. From the results, it can be observed that the dashed lines representing the conventional methods show an increasing trend in nMSE values as the number of antennas increases. The reason for this is that as the number of antennas increases, the beam-squint effect also increases, and these methods fail to perform channel estimation as they ignore this effect, leading to convergence towards high nMSE values. However, with an increase in the number of antennas, the sensed information at the BS side, where the channel estimation process takes place, increases, and the received signal level

60

becomes higher due to the array gain compared to the case with fewer antennas. Still, ignoring the beam squint effect does not provide any advantage in this regard. This once again emphasizes the importance of not neglecting this effect. On the other hand, when looking at the proposed methods represented by solid lines that perform angle estimation, it can be seen that an increase in the number of antennas generally leads to a decrease in nMSE values and achieves a performance improvement trend. These methods take into account the beam squint effect, and with an increase in the number of antennas, they utilize the advantages obtained in terms of performance, resulting in better nMSE results for the system.
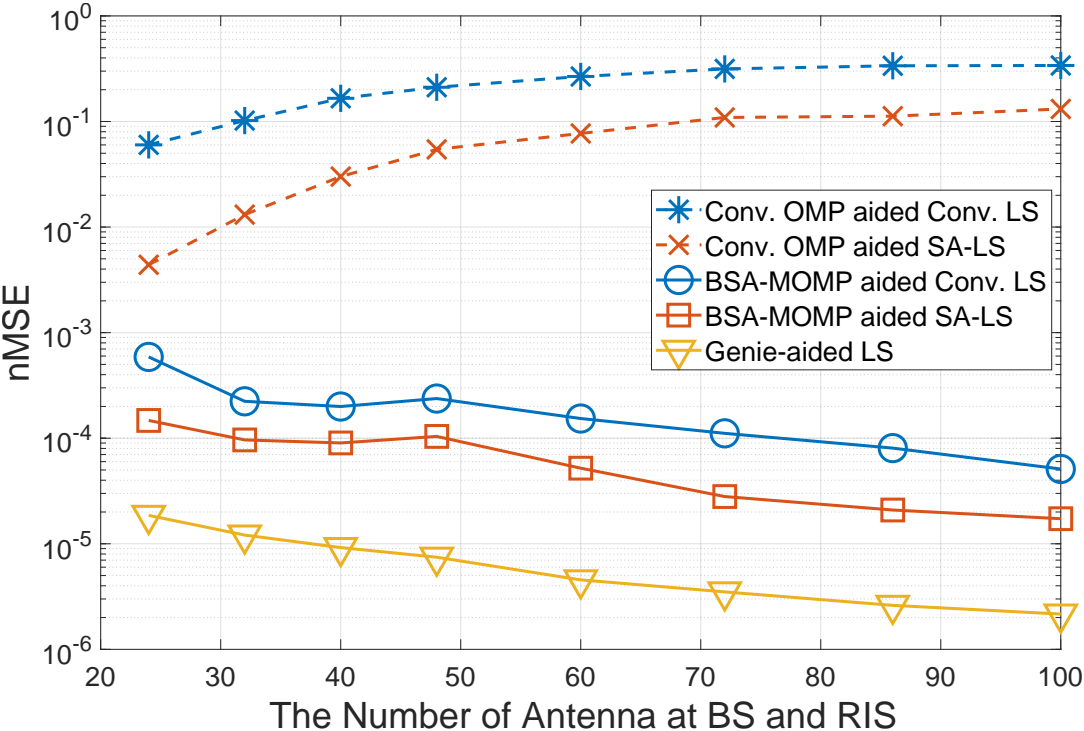

Figure 5.9: nMSE versus the number of antenna at both BS and RIS with $fc/W = 10$ and $SNR = 20\ dB$.

CHAPTER 6

CONCLUSION

6.1 Conclusions

To sum up, the main aim of this study was to find a solution to the challenge of estimating channels when using RIS in wireless communication systems. The recent emergence of RIS in the literature has shifted our focus on communication systems, moving beyond traditional transmitter and receiver manipulations to concentrate on optimizing and controlling the channel. The proposal of energy and cost-efficient optimization strategies to achieve this has made RIS even more appealing. However, this appeal comes with the challenge of channel estimation, which is a complex problem. This challenge arises from the large-scale dimensions and limited active elements on RIS, making it difficult to process signals within the device itself and necessitating processing at the communication endpoints.

Our contribution in this regard has been to tackle this intricate issue under dual-wideband channel conditions. By adopting a time division approach in the channel estimation protocol, we address the simpler gain estimation task more frequently and allocate resources smartly to the more complex angle and delay estimation tasks. By breaking down the channel estimation process into distinct phases, we also underscore the significance of RIS phase shift design within these activities. This involves using different RIS designs for angle-delay, and gain estimation, taking practical concerns such as amplitude-phase coupling into consideration.

Following this, we tested our methods under different scenarios and shared the results obtained through simulations. Looking ahead, future work could involve delving further into practical aspects, like exploring the frequency-dependent behaviors of

RIS elements. Moreover, one could consider modeling correlation as a function of symbol duration, expanding beyond the limited discussion of fully correlated and fully uncorrelated models. Additionally, incorporating this model into our estimation methods could enhance their efficiency. Lastly, due to the relatively consistent nature of angles and delays, using tracking applications instead of complete angle and delay estimation will be more efficient.

In conclusion, this study not only sheds light on the complex interaction between RIS-enhanced communication and channel estimation but also lays the groundwork for future investigations into optimizing these systems under difficult channel conditions.

REFERENCES

[1] F. Yang, P. Pitchappa, and N. Wang, "Terahertz reconfigurable intelligent surfaces (riss) for 6g communication links," *Micromachines*, vol. 13, no. 2, p. 285, 2022.

[2] M. D. Renzo, M. Debbah, D.-T. Phan-Huy, A. Zappone, M.-S. Alouini, C. Yuen, V. Sciancalepore, G. C. Alexandropoulos, J. Hoydis, H. Gacanin, *et al.*, "Smart radio environments empowered by reconfigurable ai meta-surfaces: An idea whose time has come," *EURASIP Journal on Wireless Communications and Networking*, vol. 2019, no. 1, pp. 1–20, 2019.

[3] C. Huang, A. Zappone, G. C. Alexandropoulos, M. Debbah, and C. Yuen, "Reconfigurable intelligent surfaces for energy efficiency in wireless communication," *IEEE transactions on wireless communications*, vol. 18, no. 8, pp. 4157–4170, 2019.

[4] Q. Wu and R. Zhang, "Towards smart and reconfigurable environment: Intelligent reflecting surface aided wireless network," *IEEE communications magazine*, vol. 58, no. 1, pp. 106–112, 2019.

[5] E. Basar, M. Di Renzo, J. De Rosny, M. Debbah, M.-S. Alouini, and R. Zhang, "Wireless communications through reconfigurable intelligent surfaces," *IEEE access*, vol. 7, pp. 116753–116773, 2019.

[6] A.-A. A. Boulogeorgos and A. Alexiou, "Performance analysis of reconfigurable intelligent surface-assisted wireless systems and comparison with relaying," *IEEE Access*, vol. 8, pp. 94463–94483, 2020.

[7] E. Björnson, Ö. Özdogan, and E. G. Larsson, "Reconfigurable intelligent surfaces: Three myths and two critical questions," *IEEE Communications Magazine*, vol. 58, no. 12, pp. 90–96, 2020.

[8] X. Yuan, Y.-J. A. Zhang, Y. Shi, W. Yan, and H. Liu, "Reconfigurable-intelligent-surface empowered wireless communications: Challenges and opportunities," *IEEE wireless communications*, vol. 28, no. 2, pp. 136–143, 2021.

[9] B. Wang, F. Gao, S. Jin, H. Lin, G. Y. Li, S. Sun, and T. S. Rappaport, "Spatial-wideband effect in massive MIMO with application in mmwave systems," *IEEE Commun. Mag.*, vol. 56, no. 12, pp. 134–141, 2018.

[10] B. Wang, F. Gao, S. Jin, H. Lin, and G. Y. Li, "Spatial- and frequency-wideband effects in millimeter-wave massive MIMO systems," *IEEE Trans. Signal Process.*, vol. 66, no. 13, pp. 3393–3406, 2018.

[11] M. A. ElMossallamy, H. Zhang, L. Song, K. G. Seddik, Z. Han, and G. Y. Li, "Reconfigurable intelligent surfaces for wireless communications: Principles, challenges, and opportunities," *IEEE Transactions on Cognitive Communications and Networking*, vol. 6, no. 3, pp. 990–1002, 2020.

[12] Q. Wu, S. Zhang, B. Zheng, C. You, and R. Zhang, "Intelligent reflecting surface-aided wireless communications: A tutorial," *IEEE Transactions on Communications*, vol. 69, no. 5, pp. 3313–3351, 2021.

[13] Y. Lin, S. Jin, M. Matthaiou, and X. You, "Channel estimation and user localization for irs-assisted mimo-ofdm systems," *IEEE Transactions on Wireless Communications*, vol. 21, no. 4, pp. 2320–2335, 2021.

[14] A. Taha, Y. Zhang, F. B. Mismar, and A. Alkhateeb, "Deep reinforcement learning for intelligent reflecting surfaces: Towards standalone operation," in *2020 IEEE 21st international workshop on signal processing advances in wireless communications (SPAWC)*, pp. 1–5, IEEE, 2020.

[15] R. Schroeder, J. He, and M. Juntti, "Passive ris vs. hybrid ris: A comparative study on channel estimation," in *2021 IEEE 93rd Vehicular Technology Conference (VTC2021-Spring)*, pp. 1–7, IEEE, 2021.

[16] D. Mishra and H. Johansson, "Channel estimation and low-complexity beamforming design for passive intelligent surface assisted miso wireless energy transfer," in *ICASSP 2019-2019 IEEE International Conference on Acoustics, Speech and Signal Processing (ICASSP)*, pp. 4659–4663, IEEE, 2019.

[17] D. Mishra and E. G. Larsson, "Passive intelligent surface assisted mimo powered sustainable iot," in *ICASSP 2020-2020 IEEE International Conference on Acoustics, Speech and Signal Processing (ICASSP)*, pp. 8961–8965, IEEE, 2020.

[18] J.-M. Kang, "Intelligent reflecting surface: Joint optimal training sequence and refection pattern," *IEEE Communications Letters*, vol. 24, no. 8, pp. 1784–1788, 2020.

[19] Y. Yang, B. Zheng, S. Zhang, and R. Zhang, "Intelligent reflecting surface meets ofdm: Protocol design and rate maximization," *IEEE Transactions on Communications*, vol. 68, no. 7, pp. 4522–4535, 2020.

[20] B. Zheng and R. Zhang, "Intelligent reflecting surface-enhanced ofdm: Channel estimation and reflection optimization," *IEEE Wireless Communications Letters*, vol. 9, no. 4, pp. 518–522, 2019.

[21] M. R. Akdeniz, Y. Liu, M. K. Samimi, S. Sun, S. Rangan, T. S. Rappaport, and E. Erkip, "Millimeter wave channel modeling and cellular capacity evaluation," *IEEE journal on selected areas in communications*, vol. 32, no. 6, pp. 1164–1179, 2014.

[22] K. Ardah, S. Gherekhloo, A. L. de Almeida, and M. Haardt, "Trice: A channel estimation framework for ris-aided millimeter-wave mimo systems," *IEEE signal processing letters*, vol. 28, pp. 513–517, 2021.

[23] P. Wang, J. Fang, H. Duan, and H. Li, "Compressed channel estimation for intelligent reflecting surface-assisted millimeter wave systems," *IEEE signal processing letters*, vol. 27, pp. 905–909, 2020.

[24] G. Zhou, C. Pan, H. Ren, P. Popovski, and A. L. Swindlehurst, "Channel estimation for ris-aided multiuser millimeter-wave systems," *IEEE Transactions on Signal Processing*, vol. 70, pp. 1478–1492, 2022.

[25] Z. Wan, Z. Gao, and M.-S. Alouini, "Broadband channel estimation for intelligent reflecting surface aided mmwave massive mimo systems," in *ICC 2020 - 2020 IEEE International Conference on Communications (ICC)*, pp. 1–6, 2020.

[26] Z. Wan, Z. Gao, F. Gao, M. Di Renzo, and M.-S. Alouini, "Terahertz massive mimo with holographic reconfigurable intelligent surfaces," *IEEE Transactions on Communications*, vol. 69, no. 7, pp. 4732–4750, 2021.

[27] S. Ma, W. Shen, J. An, and L. Hanzo, "Wideband channel estimation for irs-aided systems in the face of beam squint," *IEEE Transactions on Wireless Communications*, vol. 20, no. 10, pp. 6240–6253, 2021.

[28] Y. Liu, S. Zhang, F. Gao, J. Tang, and O. A. Dobre, "Cascaded channel estimation for ris assisted mmwave mimo transmissions," *IEEE Wireless Communications Letters*, vol. 10, no. 9, pp. 2065–2069, 2021.

[29] A. Abdallah, A. Celik, M. M. Mansour, and A. M. Eltawil, "Deep-learning based channel estimation for ris-aided mmwave systems with beam squint," in *ICC 2022-IEEE International Conference on Communications*, pp. 1269–1275, IEEE, 2022.

[30] Z. Wang, L. Liu, and S. Cui, "Channel estimation for intelligent reflecting surface assisted multiuser communications: Framework, algorithms, and analysis," *IEEE Transactions on Wireless Communications*, vol. 19, no. 10, pp. 6607–6620, 2020.

[31] V. Raghavan, L. Akhoondzadeh-Asl, V. Podshivalov, J. Hulten, M. A. Tassoudji, O. H. Koymen, A. Sampath, and J. Li, "Statistical blockage modeling and robustness of beamforming in millimeter-wave systems," *IEEE Transactions on Microwave Theory and Techniques*, vol. 67, no. 7, pp. 3010–3024, 2019.

[32] H. Xie, F. Gao, S. Zhang, and S. Jin, "A unified transmission strategy for tdd/fdd massive mimo systems with spatial basis expansion model," *IEEE Transactions on Vehicular Technology*, vol. 66, no. 4, pp. 3170–3184, 2016.

[33] Ö. Özdogan, E. Björnson, and E. G. Larsson, "Intelligent reflecting surfaces: Physics, propagation, and pathloss modeling," *IEEE Wireless Communications Letters*, vol. 9, no. 5, pp. 581–585, 2019.

[34] M. Najafi, V. Jamali, R. Schober, and H. V. Poor, "Physics-based modeling and scalable optimization of large intelligent reflecting surfaces," *IEEE Transactions on Communications*, vol. 69, no. 4, pp. 2673–2691, 2020.

[35] Ö. Özdogan, E. Björnson, and J. Zhang, "Performance of cell-free massive mimo with rician fading and phase shifts," *IEEE Transactions on Wireless Communications*, vol. 18, no. 11, pp. 5299–5315, 2019.

[36] S. Abeywickrama, R. Zhang, Q. Wu, and C. Yuen, "Intelligent reflecting surface: Practical phase shift model and beamforming optimization," *IEEE Transactions on Communications*, vol. 68, no. 9, pp. 5849–5863, 2020.

[37] C. Öztürk, M. F. Keskin, H. Wymeersch, and S. Gezici, "On the impact of hardware impairments on ris-aided localization," in *ICC 2022-IEEE International Conference on Communications*, pp. 2846–2851, IEEE, 2022.

[38] C. Ozturk, M. F. Keskin, H. Wymeersch, and S. Gezici, "Ris-aided near-field localization under phase-dependent amplitude variations," *IEEE Transactions on Wireless Communications*, 2023.

[39] B. Wang, F. Gao, S. Jin, H. Lin, and G. Y. Li, "Spatial-and frequency-wideband effects in millimeter-wave massive mimo systems," *IEEE Transactions on Signal Processing*, vol. 66, no. 13, pp. 3393–3406, 2018.

[40] D. Fan, F. Gao, G. Wang, Z. Zhong, and A. Nallanathan, "Angle domain signal processing-aided channel estimation for indoor 60-ghz tdd/fdd massive mimo systems," *IEEE Journal on Selected Areas in Communications*, vol. 35, no. 9, pp. 1948–1961, 2017.

[41] D. Fan, F. Gao, Y. Liu, Y. Deng, G. Wang, Z. Zhong, and A. Nallanathan, "Angle domain channel estimation in hybrid millimeter wave massive mimo systems," *IEEE Transactions on Wireless Communications*, vol. 17, no. 12, pp. 8165–8179, 2018.

[42] H. L. Van Trees, *Detection, estimation, and modulation theory, part I: detection, estimation, and linear modulation theory*. John Wiley & Sons, 2004.

[43] T. L. Jensen and E. De Carvalho, "An optimal channel estimation scheme for intelligent reflecting surfaces based on a minimum variance unbiased estimator," in *ICASSP 2020-2020 IEEE International Conference on Acoustics, Speech and Signal Processing (ICASSP)*, pp. 5000–5004, IEEE, 2020.

[44] F. Sohrabi and W. Yu, "Hybrid analog and digital beamforming for mmwave ofdm large-scale antenna arrays," *IEEE Journal on Selected Areas in Communications*, vol. 35, no. 7, pp. 1432–1443, 2017.

[45] Q. Zhu, H. Li, R. Liu, M. Li, and Q. Liu, "Hybrid beamforming and passive reflection design for ris-assisted mmwave mimo systems," in *2021 IEEE International Conference on Communications Workshops (ICC Workshops)*, pp. 1–6, IEEE, 2021.

[46] B. Deepak, R. Sankar, and S. P. Chepuri, "Channel estimation in reconfigurable intelligent surface assisted mmwave mimo systems," *arXiv preprint arXiv:2011.00900*, 2020.

Appendix A

THE PROOF OF LEMMA 1

Let us first analyze the case when θ_ℓ in the range of $(0, \frac{d_{\text{BS}}}{\lambda_c}]$. Then, (n, ℓ)-th element of $\mathbf{S}_k^H \overline{\mathbf{U}}_k$ can be expressed as

$$
\begin{aligned}
\left[\mathbf{S}_k^H \overline{\mathbf{U}}_k\right]_{n,\ell} &= \left[\mathbf{S}_k^H \overline{\mathbf{u}}_k(\theta_\ell)\right]_n \\
&= \sqrt{\frac{1}{N}} \sum_{m=1}^{N} e^{i\frac{2\pi}{N}(m-1)(n-1)\left(1+\frac{f_k}{f_c}\right)} e^{-i2\pi(m-1)\theta_\ell\left(1+\frac{f_k}{f_c}\right)} \\
&= \sqrt{\frac{1}{N}} \sum_{m=1}^{N} e^{i2\pi(m-1)\left(\frac{n-1}{N}-\theta_\ell\right)\left(1+\frac{f_k}{f_c}\right)} \\
&= \sqrt{\frac{1}{N}} \frac{1 - e^{-i2\pi\left(\frac{n-1}{N}-\theta_\ell\right)\left(1+\frac{f_k}{f_c}\right)}}{1 - e^{-i2\pi\left(\frac{n-1}{N}-\theta_\ell\right)\left(1+\frac{f_k}{f_c}\right)}}
\end{aligned}
\tag{A.1}
$$

By taking the limit as $N \to \infty$, it becomes evident that $\lim_{N\to\infty} \left[\mathbf{S}_k^H \overline{\mathbf{U}}_k\right]_{n,\ell} = 0$ when $\frac{n-1}{N} \neq \theta_l$. This is because when inequality holds, the product of $\left[\mathbf{S}_k^H \overline{\mathbf{U}}_k\right]$ becomes bounded. However when the equality is satisfied, then direct calculation in the limit yields the result of $\sqrt{N}$. That means

$$
\lim_{N\to\infty} \left[\mathbf{S}_k^H \overline{\mathbf{u}}_k(\theta_\ell)\right]_n = \sqrt{N}\delta\left(\frac{n-1}{N} - \theta_\ell\right)
\tag{A.2}
$$

As a result, there are invariably integers $n_\ell = N\theta_\ell + 1$ that satisfy the condition such that $\left[\mathbf{S}_k^H \overline{\mathbf{u}}_k\right]_{n_\ell} = \sqrt{N}$ while the rest of the elements are zero when N is sufficiently large. In simpler terms, $\left[\mathbf{S}_k^H \overline{\mathbf{U}}_k\right]$ exhibits a sparse matrix structure with power primarily focused on the coordinates (n_ℓ, ℓ) for all values of ℓ.

Let us consider the second case where θ_ℓ falls into the range of $[-\frac{d_{\text{BS}}}{\lambda_c}, 0)$. Then by

utilizing periodicity of the complex exponentials such that $e^{it} = e^{it+2\pi}$, we can re-express the equations in (A.1) shortly as

$$
\begin{aligned}
\left[\mathbf{S}_k^H \overline{\mathbf{U}}_k\right]_{n,\ell} &= \left[\mathbf{S}_k^H \overline{\mathbf{u}}_k(\theta_\ell)\right]_n \\
&= \sqrt{\frac{1}{N}} \sum_{m=1}^{N} e^{i\left[2\pi(m-1)\left(\frac{n-1}{N}-\theta_\ell\right)-2\pi(m-1)\right]\left(1+\frac{f_k}{f_c}\right)} \\
&= \sqrt{\frac{1}{N}} \sum_{m=1}^{N} e^{i2\pi(m-1)\left(\frac{n-1}{N}-\theta_\ell-1\right)\left(1+\frac{f_k}{f_c}\right)}
\end{aligned}
\tag{A.3}
$$

Similarly, when we take the limit of (A.3), then we get

$$
\lim_{N\to\infty} \left[\mathbf{S}_k^H \overline{\mathbf{u}}_k(\theta_\ell)\right]_n = \sqrt{N}\delta\left(\frac{n-1}{N} - \theta_\ell - 1\right)
\tag{A.4}
$$

As a result, there are invariably integers $n_\ell = N + N\theta_\ell + 1$ that satisfy the condition such that $\left[\mathbf{S}_k^H \overline{\mathbf{u}}_k\right]_{n_\ell} = \sqrt{N}$ while the rest of the elements are zero when N is sufficiently large. Consequently, the equations given in (A.2) and (A.4) prove the (3.6).

Appendix B

ANALYTICAL NMSE CALCULATION

$$
\begin{aligned}
\mathrm{nMSE} &\triangleq \frac{\mathbb{E}_{\mathbf{n},\boldsymbol{\gamma}}\left\{\|\mathbf{g}-\hat{\mathbf{g}}\|^2\right\}}{\mathbb{E}_{\mathbf{n},\boldsymbol{\gamma}}\left\{\|\mathbf{g}\|^2\right\}} \\[2mm]
&= \frac{\mathbb{E}_{\boldsymbol{\gamma}}\left\{\mathbb{E}_{\mathbf{n}}\left\{\|\mathbf{g}-\hat{\mathbf{g}}\|^2\right\}\right\}}{\mathbb{E}_{\boldsymbol{\gamma}}\left\{\|\mathbf{g}\|^2\right\}} \\[2mm]
&= \frac{\mathbb{E}_{\boldsymbol{\gamma}}\left\{\mathbb{E}_{\mathbf{n}}\left\{\left\|\mathbf{g}-\hat{\mathbf{W}}\hat{\boldsymbol{\gamma}}\right\|^2\right\}\right\}}{\mathbb{E}_{\boldsymbol{\gamma}}\left\{\|\mathbf{g}\|^2\right\}} \\[2mm]
&= \frac{\mathbb{E}_{\boldsymbol{\gamma}}\left\{\mathbb{E}_{\mathbf{n}}\left\{\left\|\mathbf{g}-\hat{\mathbf{W}}(\hat{\mathbf{W}}^H\hat{\mathbf{W}})^{-1}\hat{\mathbf{W}}^H\mathbf{y}^{(u)}\right\|^2\right\}\right\}}{\mathbb{E}_{\boldsymbol{\gamma}}\left\{\|\mathbf{g}\|^2\right\}} \\[2mm]
&= \frac{\mathbb{E}_{\boldsymbol{\gamma}}\left\{\mathbb{E}_{\mathbf{n}}\left\{\|\mathbf{g}-\mathbf{P}_{\hat{\mathbf{W}}}(\mathbf{g}+\mathbf{n})\|^2\right\}\right\}}{\mathbb{E}_{\boldsymbol{\gamma}}\left\{\|\mathbf{g}\|^2\right\}} \qquad\qquad\text{(B.1)} \\[2mm]
&= \frac{\mathbb{E}_{\boldsymbol{\gamma}}\left\{\mathbb{E}_{\mathbf{n}}\left\{\left\|\mathbf{P}_{\hat{\mathbf{W}}}^{\perp}\mathbf{g}-\mathbf{P}_{\hat{\mathbf{W}}}\mathbf{n}\right\|^2\right\}\right\}}{\mathbb{E}_{\boldsymbol{\gamma}}\left\{\|\mathbf{g}\|^2\right\}} \\[2mm]
&= \frac{\mathbb{E}_{\boldsymbol{\gamma}}\left\{\mathrm{Tr}\left\{\mathbf{P}_{\hat{\mathbf{W}}}^{\perp}\mathbf{g}\mathbf{g}^H\mathbf{P}_{\hat{\mathbf{W}}}^{\perp}+N_0\mathbf{P}_{\hat{\mathbf{W}}}\right\}\right\}}{\mathbb{E}_{\boldsymbol{\gamma}}\left\{\mathrm{Tr}\left\{\mathbf{W}\boldsymbol{\gamma}\boldsymbol{\gamma}^H\mathbf{W}^H\right\}\right\}} \\[2mm]
&= \frac{\mathbb{E}_{\boldsymbol{\gamma}}\left\{\mathrm{Tr}\left\{\mathbf{P}_{\hat{\mathbf{W}}}^{\perp}\mathbf{W}\boldsymbol{\gamma}\boldsymbol{\gamma}^H\mathbf{W}^H\mathbf{P}_{\hat{\mathbf{W}}}^{\perp}+N_0\mathbf{P}_{\hat{\mathbf{W}}}\right\}\right\}}{\mathbb{E}_{\boldsymbol{\gamma}}\left\{\mathrm{Tr}\left\{\mathbf{W}\boldsymbol{\gamma}\boldsymbol{\gamma}^H\mathbf{W}^H\right\}\right\}} \\[2mm]
&= \frac{\mathrm{Tr}\left\{\mathbf{P}_{\hat{\mathbf{W}}}^{\perp}\mathbf{W}\mathbf{R}_{\boldsymbol{\gamma}}\mathbf{W}^H\mathbf{P}_{\hat{\mathbf{W}}}^{\perp}\right\}+N_0 LJ}{\mathrm{Tr}\left\{\mathbf{W}\mathbf{R}_{\boldsymbol{\gamma}}\mathbf{W}^H\right\}} \\[2mm]
&= \frac{\mathrm{Tr}\left\{\mathbf{W}^H\mathbf{P}_{\hat{\mathbf{W}}}^{\perp}\mathbf{W}\mathbf{R}_{\boldsymbol{\gamma}}\right\}+N_0 LJ}{\mathrm{Tr}\left\{\mathbf{W}^H\mathbf{W}\mathbf{R}_{\boldsymbol{\gamma}}\right\}}
\end{aligned}
$$